A Density Functional Theory Study of Copper-Doped Nickel Oxide Supercells

Galen David Crumpton

MSc by Research

University of York
School of Physics, Engineering and Technology

December 2023

Abstract

Understanding the effects of defects on the properties of transition metal oxides is of great importance to the chemical, biological and sustainability industries. Nickel oxide is one such material that is widely used in various forms, and continues to be studied; most notably with vacancies and dopants both being introduced into the material through experiment. The electronic properties of bulk NiO have been calculated using the RSCAN and PBE XC-functionals, with particular focus on spectral and optical properties.

Additionally, 108-atom supercells have been constructed, with intrinsic and extrinsic defects being placed in the supercell. The copper-doped supercell has been studied for various copper atom positions and concentrations. The doping site type altered the electronic properties in different ways, with clear n-type behaviour being exhibited by substitution on oxygen sites and interstitial doping. This increased n-type behaviour and narrowing of the band gap suggests that careful engineering of the chemical environment to favour forming these defects will produce a material with higher conductivity and charge transfer rates, which is essential for photocathode applications.

By varying the distance between dopant Cu atoms, it was found that it is energetically favourable for the Cu atoms to be closer together than further apart, with an energy difference of approximately 70 meV. Additionally, the preferential alignment of multiple Cu atom dopants was found to be along the same [111] plane.

An exploratory study into the different stable compounds containing Ni, Cu and O has been carried out, with a 2D ternary convex hull being plotted to investigate these compounds' stability. There is only one predicted stable compound containing all three species, the rhombohedral structure Ni_9CuO_{10}.

Declaration

I declare that all content within this thesis is original work and that I am the sole author. This work has not been submitted to this university or any other in the past for the award of a degree or other qualification. All sources used within this piece of work are acknowledged as references. Additionally, I can confirm that this thesis follows all submission guidelines, including the minimum 10,000 word count.

Galen David Crumpton
December 2023

Acknowledgements

I would like to acknowledge my supervisors Dr. Vlado Lazarov and Dr. Phil Hasnip for their crucial help and support throughout my degree. I would also like to acknowledge the help of my colleagues in the school of physics, engineering and technology and the nanocentre, Julio Nascimento, Scott Donaldson, Dr. Robert Lawrence, and Dr. Peter Byrne for helping me get setup with CASTEP. I also give acknowledgement to the teams that run the Viking, Young, and ARCHER2 computing clusters, without which this study would not have been possible. Finally I'd like to thank my family for the love and support they have given me throughout my degree. Especially my grandparents, mum, dad and sister. I dedicate this work to you all.

Table of contents

List of figures

List of tables

Chapter 1

Introduction

1.1 Transition Metal Oxide Applications

1.1.1 Current TMO Applications

Transition metal oxides (TMOs) have started to see widespread use after decades of research into their properties. They have found use as nanoparticles of different geometries, nanotubes and thin films in the pharmaceutical, energy production and catalysis industries. More recently, there has been an interest in the doping of TMOs to alter their bulk properties. For example, doping manganese or cobalt into zinc oxide nanoparticles to alter the photocatalytic abilities for use in the destruction of organic waste [1].

A current area of intense research is that of using TMOs in the fight against climate change. A vast number of TMO structures are being actively studied to investigate their uses as rechargeable battery cathodes, such as $LiCoO_2$ and $LiFePO_4$ [2][3]. Alongside energy storage, TMOs are also being used in solar and wind technologies. There is always the possibility of finding new TMO structures that are lower cost or more efficient than the current generation, and thus both experiment and theory are coming together to continue this search.

1.1.2 Nickel Oxide

Nickel oxide, (NiO) is a TMO which has been closely studied for use in the previously mentioned industries. Nickel itself has an electron configuration of $[Ar]3d^8 4s^2$, with the partially filled 3d orbital leading to an overall magnetic spin moment.

NiO is also known to be a Fm-3m space group face-centred cubic (FCC) crystal Mott insulator and a type-II anti-ferromagnetic material with a high Néel temperature of 524K [4][5].

These useful magnetic properties, natural abundance and low cost have lead to the particular interest in its use in the spintronics field of study [6].

In order to alter the properties of NiO, much like that of other TMO nanoparticles, the material can be doped with another metal. There has been extensive work doping NiO with the group one alkali metals such as lithium and potassium [7][8]. Group one metals have been found to improve the p-type conductivity and thus hole transport capabilities for their use with perovskite materials. The main drawbacks of using group one metals in this way is their expense, environmental impact from being mined and also their chemical instability.

As an alternative to group one metal dopants, there has also been a lot of research investigating the TM doping of nickel oxide. Copper for example is particularly suitable due to its electronic similarity to nickel. Furthermore, copper is a non-magnetic element and incorporating it into NiO has been shown to affect the magnetic properties of NiO nanoparticles, changing them from anti-ferromagnetic systems to weakly ferromagnetic at room temperature [9]. The doping concentration also has a large impact on the properties of the material. Incorporating copper atoms into the structure in the place of nickel is expected to push the material to being either more of a p-type or n-type donor depending on the system [10]. This is of particular importance in the use of Cu-doped NiO as a hole layer for perovskite materials, as doping is critical for hole transportation layers in solar cells [11].

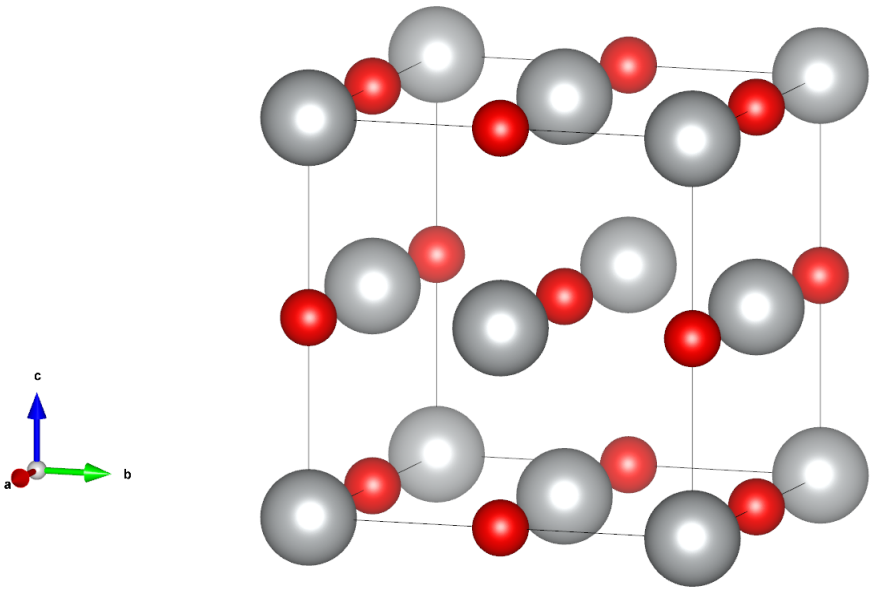

Fig. 1.1 The FCC unit cell of NiO, with nickel atoms in silver and oxygen atoms in red.

1.2 Motivations for Computational Modelling

In the last few decades, computer simulations of materials have improved considerably, alongside the efficiency and power of computer hardware. Capitalising on this increase in power, quantum scale simulations have been getting more and more advanced, with the *ab initio* method of density functional theory (DFT) seeing an increase in its effectiveness and widespread use in almost every field of science that requires atomistic or molecular modelling.

The ability to model a material computationally and perform virtual experiments upon it is integral to understanding results produced from experiments. New materials that have not yet been synthesised can be analysed through first principle methods, eventually leading to the synthesis and testing of brand new materials with interesting properties. Indeed, DFT has been instrumental as an exploratory technique in finding effective new dopants for NiO to improve its properties [12].

Chapter 2

Density Functional Theory

2.1 Introduction

In order to investigate the electronic properties of new or theoretical materials, many of which cannot be investigated in a lab, a computational method to simulate these materials is necessary. The discovery of quantum mechanics enabled scientists to accurately probe the properties of materials at microscopic levels, such as solving the wavefunction for a hydrogen atom [13]. All equations within this chapter use Hartree atomic units, with $\hbar = 1$, $e = 1$, $m_e = 1$, and $\frac{1}{4\pi\varepsilon_0} = 1$.

2.2 Time-Independent Schrödinger Equation

The time-independent Schrödinger equation (TISE) is one of the most important formulations in quantum theory, being able to solve all of the energy states of chemical systems, such as a single hydrogen atom. As powerful as this equation is however, it is unfeasible to be used for systems that contain multiple electrons and larger nuclei. The more complex interactions between multiple electrons and multiple nuclei need to be taken into account, leading to a dramatic increase in the computational expense of solving the wavefunction. The general form of the TISE is given by $\hat{H}\psi = E\psi$ [14]. The Hamiltonian, $\hat{H}$ in this case encapsulates all nuclei-nuclei, electron-nuclei and electron-electron interaction energies.

2.2.1 Born-Oppenheimer Approximation

One of the key issues with the many-body problem is that describing the wavefunction of an atom involves the consideration of the wavefunctions of both the electrons and the nucleus. To simplify this problem, it was proposed by Born and Oppenheimer in 1927 to separate out the energetics of the nucleus and that of the electrons and treat them as separate problems to solve

[15]. This is possible due to the velocity of nuclei being much lower than that of the electrons as nuclei are much heavier than the electron. It has been observed that in the frame of reference of nuclei, any electrons will instantaneously respond to any changes in distance between it and the nuclei. This assumption allows for the kinetic energy term in the many-body Hamiltonian for the nucleus to be ignored. After considering the Born-Oppenheimer approximation, the ground state energy equation of the system becomes

$$\left[-\frac{1}{2}\sum_{i=1}\nabla_i^2 + T_n + V_{n-n} + \sum_{i=1} V(\mathbf{r}_i) + \frac{1}{2}\sum_{i\neq j}\frac{1}{|\mathbf{r_i}-\mathbf{r_j}|}\right]\psi = E\psi \tag{2.1}$$

with the first term describing the electron kinetic energy, the second and third terms the nuclear kinetic energy and nuclei-nuclei interaction potential energy respectively, which are both constants due to the Born-Oppenheimer approximation, the fourth term being the electron-nuclei interaction potential energy, and the final term the electron-electron interaction potential energy [16].

2.3 The Hohenburg-Kohn Theorems

The work by Hohenburg and Kohn in 1964, the Hohenburg-Kohn theorems, form the foundation upon which the principles of DFT have been built [17].

Hohenburg-Kohn Theorem I

The first theorem states that the external potential that the system of ground state particles are in, $V(\mathbf{r})$, is used to determine the ground-state particle density, $\rho(\mathbf{r})$. The fact that the electron density is able to give the ground state energy of the system leads to a reduction in the dimensions involved in the many-body problem, with a 3D system of N electrons, each with 3N coordinates in space being reduced to just 3 coordinates. The key to this implementation is the use of functionals of the electron density.

$$\hat{E}\left[\rho\left(\mathbf{r}\right)\right] = \hat{F}\left[\rho\left(\mathbf{r}\right)\right] + \int V\left(\mathbf{r}\right)\rho\left(\mathbf{r}\right)\cdot d\mathbf{r} \tag{2.2}$$

Hohenburg-Kohn Theorem II

The second theorem states that a universal functional for the energy, $E[n]$ can be defined in terms of the particle density, $\rho(\mathbf{r})$. This functional is said to be valid for any local potential,

$V(\mathbf{r})$. The exact ground state energy of the system is the global minimum value of the functional. Additionally, the particle density, $\rho(\mathbf{r})$ that minimizes this functional is the ground-state particle density, $\rho_0(\mathbf{r})$.

2.4 The Kohn-Sham Equations

The Kohn-Sham approach outlined by Kohn and Sham in 1965 builds upon the approach of the Hohenburg-Kohn theorems [18]. Instead of seeing the system as a many-body particle problem, the Kohn-Sham approach defines an auxiliary system based on an independent particle problem. The auxiliary system in question contains all of the information for tackling the problem, including the nuclear potentials, Coulomb interactions, and kinetic energies. The complex interactions between electrons are incorporated into a new functional, $\hat{E}_{XC}[\rho(\mathbf{r})]$.

The ground-state energy, $\hat{E}[\rho(\mathbf{r})]$ in the Kohn-Sham formulation is defined as

$$\hat{E}[\rho(\mathbf{r})] = \hat{T}[\rho(\mathbf{r})] + V(\mathbf{r}) + V_H(\mathbf{r}) + V_{XC}(\mathbf{r}) \tag{2.3}$$

with $\hat{T}[\rho(\mathbf{r})]$ being the kinetic energy of a non-interacting gas, and $V(\mathbf{r})$ being the external potential [19].

The Hartree potential, V_H and the exchange-correlation potential, V_{XC} is defined as

$$V_H(\mathbf{r}) = \int \frac{\rho(\mathbf{r}')}{|\mathbf{r}-\mathbf{r}'|} d^3\mathbf{r}' \tag{2.4}$$

$$V_{XC}(\mathbf{r}) = \frac{\delta \hat{E}_{XC}[\rho(\mathbf{r})]}{\delta \rho(\mathbf{r})} \tag{2.5}$$

This new universal exchange-correlation functional can theoretically be used to determine the exact ground-state properties of any material. However, in practice this functional is used in approximate forms, usually with great success. In fact, the search for better forms of $\hat{E}_{XC}[\rho(\mathbf{r})]$ is still a very much active area of research to this day.

2.5 Exchange-Correlation Functionals

The key element of DFT is the fact that the exact exchange-correlation functional is unknown. Thus, there are numerous different exchange-correlation functionals available for use in different materials, depending on the level of theory required for the properties being calculated.

2.5.1 Local Density Approximation (LDA) and Generalised Gradient Approximation (GGA) Functionals

The original, simplest XC-functional, the Local Density Approximation (LDA) was theorised in 1965 by Kohn and Sham. LDA treats the atom as a homogeneous electron gas, which was reported to calculate electronic properties of certain materials, such as silicon, remarkably well [20]. However, for the vast majority of materials LDA is not sufficient for rigorous calculations. It has often been found that LDA overbinds the atoms, leading to inaccurate bond-lengths. A major advantage however of LDA is that it is the fastest XC-functional to use for computation time.

As there are many materials for which LDA is not sufficient, a new type of XC-functional was needed; Generalised Gradient Approximation functionals (GGAs) are the next step up in complexity. One of the most established of these being the PBE, formulated by Perdew *et al* [21]. GGAs not only consider the charge density, but also its gradient. This correction can help prevent over-binding of atoms, but has been shown to under-bind slightly in some cases instead.

2.5.2 Meta-Generalised Gradient Approximation (mGGA)

Meta-Generalised Gradient Approximation (mGGAs) push the concepts invoked in the GGAs one step further. These XC-functionals take into account the orbital kinetic energy density alongside the electron density and its gradients.

SCAN

One of the most prominent mGGA functionals is the Strongly Constrained and Appropriately Normed (SCAN) functional developed by J. Sun *et al* [22]. SCAN is widely accepted to produce agreeable results in the case of semiconductors and metal oxides. The key difference with SCAN functionals is the use of the isorbital indicator function, calculated with $\alpha = \frac{\tau - \tau_w}{\tau_U}$, which aids in the detection of local bond types, namely metallic, covalent, and weak.

RSCAN

The regularised SCAN functional (RSCAN) was later developed, which fixed a major issue with SCAN, namely that derivatives of α with respect to electron density show divergent behaviour with rapidly decreasing electron densities [23]. It was proposed that there should be an additional regularising function, $\alpha' = \frac{\alpha^3}{\alpha^2+\alpha_r}$, where $\alpha_r = 1 \times 10^{-3}$ and is a regularising constant. This version of the isorbital indicator function differs from the original at small values.

2.6 Calculating the Hubbard U

2.6.1 The Necessity of the Hubbard U

The Hubbard U value is often needed to correct the energy levels that the electrons can occupy. For large band gap metal oxides such as NiO, LDA and GGA based XC-functionals on their own are unable to correctly calculate that metal oxides generally have large band gaps, with NiO having an estimated experimental band gap of 3.6-4.0 eV [24][25]. This wide range arises from the variation in purity of lab-grown NiO crystals, with defects and surface morphology contributing to the variation of the experimental band gap measurement [26]. This discrepancy is known to cause inaccuracies in calculated electronic properties as a result, with insulators and semiconductors often being miscalculated to be metallic. In order to correctly show computationally that there is a band gap in materials such as these, a factor known as the Hubbard U is often used alongside the DFT calculation, known as DFT+U [27]. The cause of this issue is from the self-interaction error, which is also often referred to as the electron delocalisation error [28]. The Hubbard U value attempts to resolve this issue by increasing the localisation of these troublesome states. The Hubbard-like interaction is introduced to only these specified orbitals, with the rest of the DFT calculation being left unaffected. Most DFT codes by default apply both the U and J parameters, allowing the application of an effective Hubbard U value given by $U_{eff} = U - J$ [29].

2.6.2 The Linear Response Method

As many materials have already had the U computed, it's relatively easy to find a sensible range of U values for a given material and system. While this method can give good enough results, there exists a few other methods to correctly find the U value for the system being modelled without resorting to fitting the result to experiment.The use of these improved methods thus saves time and computational expense from having to run many calculations with varying U

values. Additionally, there is the added advantage of obtaining accurate U values for the system of atoms for which the U is applied to in your system that reproduces the known properties.

One of the more rigorous methods to calculate the Hubbard U parameter is by performing a linear response calculation. It was decided to use the plane-wave code Quantum Espresso (QE) to perform this calculation [30]. This approach unfortunately has the downside of the calculated U parameter technically not being transferable to CASTEP due to the fact that QE uses a different pseudopotential format. This being the case however, using the QE-calculated Hubbard U parameter in CASTEP, should it give a realistic band gap, is still more rigorous than just fitting U to experimental data. The linear response method implemented by QE is based upon the works of Cococcioni and Gironcoli

$$U = \frac{\partial \alpha_I^{KS}}{\partial q_I} - \frac{\partial \alpha_I}{\partial q_I} = \chi_0^{-1} - \chi^{-1} \tag{2.6}$$

with α_I being the alpha value, q_I the Hubbard occupancy, χ_0 being the full linear response function and χ being the linear response function to the perturbation in the system due to the applied Hubbard α [31].

2.7 Bloch's Theorem

An idea integral to plane-wave DFT codes, including CASTEP, is that of periodic cells. By assuming periodic boundary conditions of a unit cell, one can calculate electronic properties of bulk materials. Bloch's theorem states that for a periodic potential, the electron density is also periodic [32]. This allows for the creation of wavefunctions that are also periodic, like thus

$$\phi_k = e^{i\mathbf{k}\cdot\mathbf{r}} u_k(\mathbf{r}) \tag{2.7}$$

where $e^{i\mathbf{k}\cdot\mathbf{r}}$ is a plane-wave, and $u_k(\mathbf{r})$ is also periodic in space, with the same periodicity as the cell. Satisfying this theorem allows for each k-point, a grid of which is used to sample the Brillouin zone, to be solved independently, which is one of the keys to speeding up computational calculations. The fact that u_k is periodic in 3D space means that it can be written as a Fourier series

$$u_k(\mathbf{r}) = \sum_G c_{Gk} e^{i\mathbf{G}\cdot\mathbf{r}} \tag{2.8}$$

$$E_{cut} = |\mathbf{G}|^2 \tag{2.9}$$

where for equation 2.8 c_{GK} are the complex Fourier coefficients, and $\mathbf{G}$ is a reciprocal lattice vector. The $e^{i\mathbf{G}\cdot\mathbf{r}}$ is also known as a plane-wave, and is a key component in determining the cut-off energy of DFT calculations, which will be explored in detail in the convergence testing section of this thesis. The equation 2.9 shows the relationship between the cut-off energy i.e. the maximum plane-wave energy allowed, and $\mathbf{G}$.

The KKR Green's Function Method

There exists many alternatives to plane-wave DFT methods which use different basis sets or investigate other quantities such as the Green's function as opposed to the Bloch wave function. One such method is the multiple-scattering theory based Korringa–Kohn–Rostoker (KKR) method [33]. This method differs from plane-wave DFT by dividing the system into non-overlapping spheres to represent the potential surrounding each atom instead of using pseudopotentials and plane waves in the interstitial regions. Additionally, the coherent potential approximation (CPA) can be used alongside the KKR method for alloys, which implements an approximation to the full Green's function utilising an ensemble average of the alloyed atoms [34]. Both plane-wave and Green's function methods have been shown to have comparable accuracy in computing the band structure of semiconductors, and thus the plane-wave method has only been considered for this study.

2.8 Pseudopotentials

As detailed by Bloch's theorem, the computed wavefunction can be described by a sum of plane-waves. The wavefunctions of electrons close to the core of the atom tends to oscillate more due to the ionic potential. The fact that this creates potentially many nodes and anti-nodes means that a vast number of plane-waves are needed to accurately model these oscillations, often reaching energies in the order of hundreds of keV's. This would make the computational cost of calculations unviable.

To solve this, plane-wave DFT codes use pseudopotentials to encapsulate the main properties of the wavefunction. As it is the valence electrons that mostly contribute to the chemical properties of a material, the approximation can be made to largely ignore the tightly-bound core states.

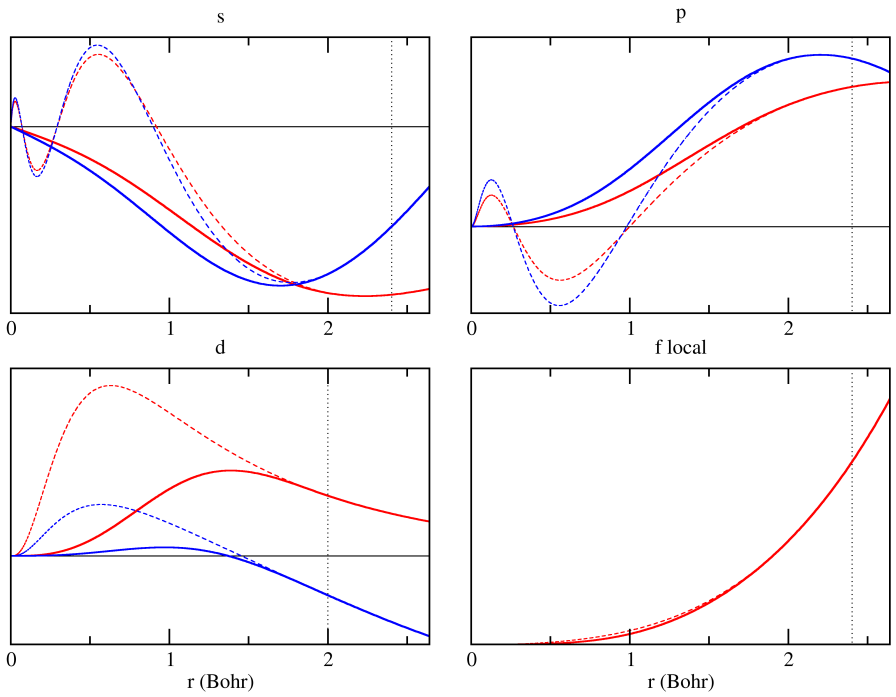

Fig. 2.1 The nickel s, p, and d radial Kohn-Sham orbitals are shown by the dashed line, and the pseudowavefunctions are shown with a solid line. The f local plot describes the computed local potential.

The many-body wavefunctions and pseudopotentials for nickel clearly show the oscillation of the wavefunction in both the s and p orbitals, and how the pseudopotential largely ignores these oscillations. The fact that the pseudopotentials contain fewer nodes means that considerably fewer plane-waves are required to capture the required shape.

2.9 Limitations of DFT

As powerful as DFT is as a tool, there are numerous limitations with DFT. Generally, DFT calculations assume a non-physical system temperature of 0K. Indeed, it is very difficult to capture temperature information of materials in DFT due to one of the foundational approximations, the Born-Oppenheimer approximation. It is impossible to describe temperature without assuming motion of atomic nuclei.

Another key problem when performing calculations that require electronic excitation is that time dependence must be brought back into calculations. To this end, there is the relatively new field of time-dependent DFT (TDDFT). TDDFT is considerably more expensive than regular DFT, and currently has poor support for metallic systems on most DFT codes.

Furthermore, care must be taken when investigating charged defects within supercells. By introducing a charged defect into a supercell, the periodicity of the system means that each charged defect will interact with its neighbouring cells in every dimension. Therefore, any supercells that are long and thin are generally unsuited to these kinds of calculations from Coulomb repulsion forces having a strong effect along one or two axes.

2.10 Using CASTEP

2.10.1 Introduction

CASTEP is an *ab initio* DFT calculation software package [35]. The main purpose of all DFT software is to solve the Kohn-Sham equations previously discussed and calculate the ground state energy at 0K. CASTEP is also able to calculate spectral properties such as band structures and the density of states (DOS) for example. Thermo-electric properties can also be calculated by carrying out phonon calculations.

2.10.2 Convergence Testing

It's important to ensure that any values of interest obtained from a DFT calculation are sufficiently converged under a certain self-consistent field (SCF) tolerance. This is performed by varying one parameter and keeping the other parameters fixed, and then changing the parameter under investigation and repeating until a suitable range of values of what is being converged has been tested for each parameter.

In this study the main values of interest are the ground state energy and the internal forces. The main parameters which are varied include those responsible for the plane-wave basis, namely the cut-off energy, the Monkhorst-Pack grid value and the fine grid. The plane-wave cut-off and the k-point grid values are orthogonal to each other and so can be varied independently while the other value is fixed. However the fine grid depends on the cut-off energy and so the fine grid needs to be tested once a well-converged cut-off energy is known.

2.10.3 Geometry Optimisation

Before any data can be collected on material, it is paramount that the cell is 'relaxed'. In other words, the ground state energy of the system must be minimised alongside the ionic positions being optimised for the structure in order for the calculations to represent reality. CASTEP has functionality like all DFT codes to relax the cell using a variety of algorithms for doing so.

The default method and the most widely used one is the limited-memory Broyden-Fletcher-Goldfarb-Shanno (LBFGS) algorithm. This method is a low-memory variant of the original sophisticated BFGS algorithm, and is comparable in terms of performance for most systems.

2.10.4 Density of States (DOS)

The electronic density of states (DOS) is frequently used in the study of the electronic structure of a material. DOS can give information about the chemical bonding and the number of energy states available per unit cell for certain energies. Most DFT codes, including CASTEP, allow for spin-polarised calculations and thus spin-polarised DOS can be calculated for magnetic materials such as NiO. Additionally, the DOS and band structure can show the differences between insulators, semiconductors and metals from the calculation of theFermi level, E_F, conduction band minimum (CBM), and valence band maximum (VBM). The projected DOS (PDOS) can also be calculated by CASTEP, showing the orbitals responsible for the various energy states.

The DOS is simply calculated by integrating the calculated electron density in reciprocal space, which is possible due to the plane-wave nature of the electron density in plane-wave DFT.

CASTEP comes bundled with the post-processing tool OptaDOS which can separate and plot the total DOS (TDOS) and PDOS[36]. Additionally, OptaDOS has the capability to calculate a more accurate Fermi energy by applying adaptive broadening to the CASTEP generated value.

2.10.5 Electron Energy Loss Spectroscopy (EELS)

A key experimental technique for studying the electronic structure of materials aside from the DOS is electron energy loss spectroscopy (EELS). Data for this is often collected via a detector attached to an electron microscope.

CASTEP is able to calculate both low-loss spectra and core-loss, with the latter requiring some modification to the .cell file to specify which ion and orbital is to have the electron removed. Unfortunately, without the use of the more advanced technique of time-dependent DFT (TDDFT), certain core edges are not sufficiently accurate when compared with experiment. The main edge investigated in this study is the nickel L2,3 edge for NiO.

2.10.6 Optics

Alongside spectral calculations, CASTEP has functionality to compute optical properties of a material. The incident photon energy over a wide range is used, giving insight into how a material interacts with low energy photons such as infra-red, through to visible and all the way up to typical ultra-violet (UV) energies.

Chapter 3

Bulk NiO Calculations

3.1 Introduction

To understand the basic electronic properties of bulk NiO, calculations must be performed on the primitive cell. Additionally, before any calculation is carried out, the best basis set must be determined through convergence testing. This chapter details the convergence testing of NiO and CuO, and finally details the theoretical spectral properties of bulk NiO. Furthermore, details of the method used to calculate the optimal Hubbard U value for nickel is elaborated upon, alongside a comparison of the spectral results using PBE+U vs RSCAN. All calculations were carried out on the Viking, Young, and ARCHER2 computer clusters.

3.2 Computational Methodology

3.2.1 The Rhombohedral Primitive Cell

The convergence testing was carried out on the smallest unit cell that included the type-II antiferromagetic (AFM) nature of NiO. Antiferromagnets are defined as having a zero net magnetic moment which arises due to symmetry. Type-II AFM structures have atoms arranged such that each [111] plane throughout the crystal, the atoms are all spin up or spin down [37]. In order to achieve this desired structure, a rhombohedral unit cell of NiO was constructed from the FCC unit cell obtained from MaterialsProject.org, with the Ni atom at the origin being set to spin up, and the other Ni atom set to spin down [38].

The lattice parameter for the rhombohedral cell was obtained by the equation $a_{rhom} = a_{fcc}\sqrt{\frac{3}{2}}$. The angle of the unit cell was determined by generating $2\times2\times2$ supercell of the FCC structure and using trivial trigonometry to find the unit cell angle. Rhombohedral systems have a crystal lattice defined by: $a = b = c$ and $\theta_1 = \theta_2 = \theta_3$. For NiO, a lattice parameter

of $a = 5.16$ Å and $\theta = 33.6°$ was used. For CuO, the lattice parameter was worked out to be $a = 5.18$ Å, with θ being the same as for NiO.

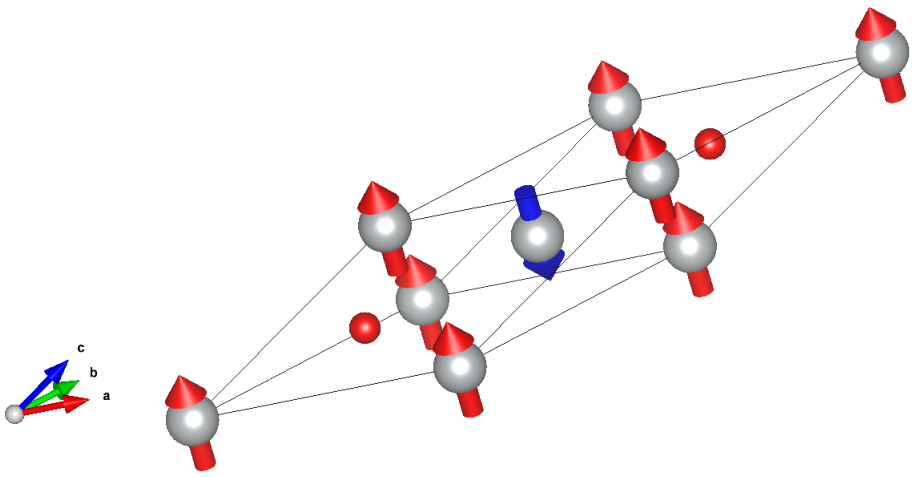

Fig. 3.1 The rhombohedral primitive cell used to perform initial spectral calculations. There are 2 Ni and 2 O atoms, with nickel atoms being shown in silver and oxygen atoms in red. The spin up states are shown in red and spin down shown in blue.

The calculated spins on the Ni atoms were initialised in the .cell file as +/-2μ_B. The expected local magnetic spin moment of individual Ni atoms is expected to be approximately 1.9μ_B [39][40]. To obtain as accurate a spin as possible with DFT, it's necessary to set the spin to be higher than the experimental value due to the fact that the correct spin moment is more easily found when the larger initial value is overestimated.

3.2.2 NiO 3×3×3 Supercell

In order to investigate the effects of defects, a much larger supercell was also required. The 4 atom rhombohedral cell was repeated in all three dimensions, three times to create the 3×3×3 NiO supercell. This supercell has much more clear spin up and spin down [111] plane arrangements. The bonds have been hidden in figure 3.2 to make the atomic/spin arrangement more clear. This supercell consists of 108 atoms in total, 54 Ni and 54 O. The lattice parameter is three times that of the unit cell, 15.5 Å with the cell angles being the same. This is the base supercell into which Cu atoms and vacancies were introduced.

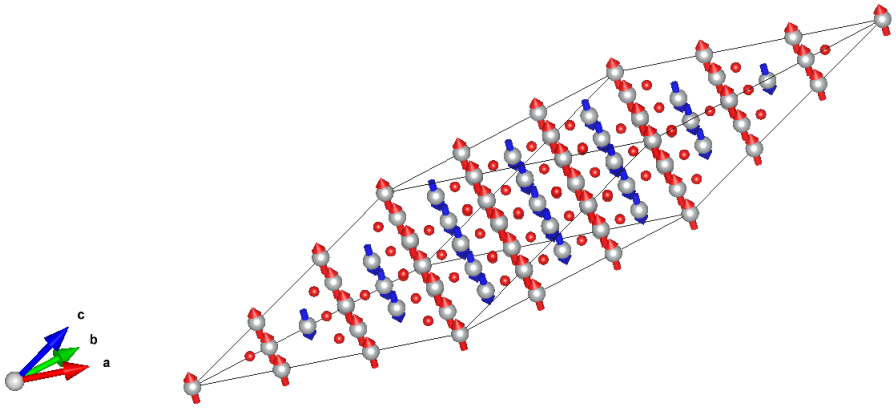

Fig. 3.2 The 108 atom NiO supercell, with added spin states to demonstrate the type-II AFM nature. Spin up states are represented in red and spin down in blue.

3.2.3 Convergence Testing

Before testing was carried out on the NiO and CuO primitive cells, a rough cut-off energy convergence graph was obtained from running a test geometry optimisation calculation and turning on output printing mode from the pseudopotential declaration string in the .cell file. The reasoning behind this step is to figure out a decent range of cut-off energies to test, starting from a minimum value that gives good enough results. A minimum of 500 eV for convergence testing was ascertained from the plot shown in figure 3.3.

Once the NiO and CuO primitive cells were constructed, the optimal basis set could be found. The convergence testing was carried out using the Python-based convergence testing script bundled with CASTEP, called 'castepconv'. It was decided that a cut-off energy range of 500-2000 eV would be sufficient to investigate the cut-off convergence. Castepconv also allows for the convergence of the k-points grid to be tested. A range of $4\times4\times4$ to $20\times20\times20$ was decided to be a large enough range for this.

Separate to cut-off and k-points convergence, the grid scale and fine grid scale parameters were also tested. These parameters are especially important when using ultra-soft pseudopotentials like in this study as ultra-soft pseudopotentials often require larger grid and fine grid scales than the default values of 1.75 and 1.0 respectively. This was tested by repeating the convergence tests with different grid scales and fine grid scales and comparing them all. Finally, an important part of this study is the comparison of the regular GGA results to that of mG-

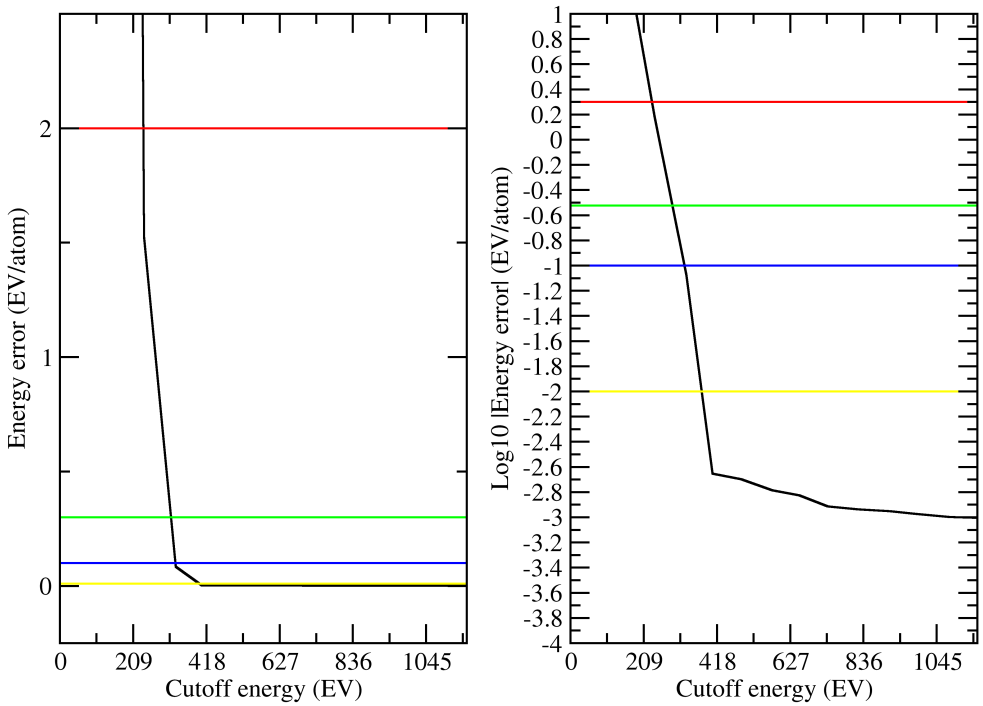

Fig. 3.3 The rough cut-off energy convergence test for nickel.

GAs. This means that all convergence tests must be carried out using both PBE and RSCAN XC-functionals.

3.2.4 Hubbard U Calculation

Often for DFT+U calculations, a well-tested literature value for U is used. The issue with this is that U strongly depends on the system it's being applied to, so U is not transferable to every system it is used in.

The best value of U was calculated in this project using the rigorous linear response method. The DFT program QuantumEspresso (QE) was used to compute these values as it contains the linear response calculation script, 'hp.x', implemented by I. Timrov *et al* [41].

The unfortunate downside of using QE over CASTEP is that both programs use slightly different PBE pseudopotentials for nickel and oxygen. This means that the U value calculated in QE is technically not transferable to CASTEP. This aside, the assumption was made that the computed value of U using the QE PBE pseudopotentials will be close enough to the

CASTEP PBE pseudopotentials. Furthermore, so long as the U value produces a band gap that is comparable to experiment then the U value is still adequate for the calculations.

In order to test the linear response calculated U, the U value was varied between 1.0-10 eV in 0.5 eV steps. The electronic band gap and broadened Fermi energy from the DOS is then calculated using OptaDOS. The linear response U results are then plotted on this curve.

3.2.5 Spectral Calculations

Once the crystal has been relaxed, the optimised structure would then be used to calculate the band structure and density of states of the primitive cell. The shape of the Brillouin zone (BZ) shown in figure 3.4 is FCC-based due to the fact that the rhombohedral primitive cell is derived from the FCC supercell. The BZ k-path is the sampling path taken between the points of high symmetry, and is used to display band structures. The BZ diagram was produced using the SeeK-Path website, which in turn generates the BZ model with the aid of the crystal symmetry software library, Spglib [42][43].

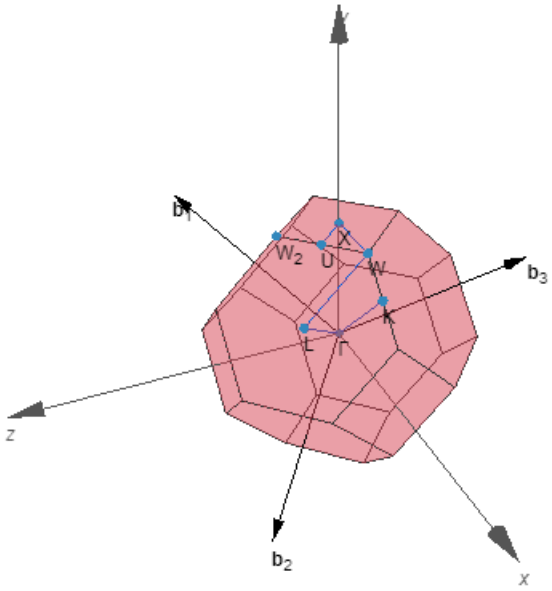

Fig. 3.4 The BZ and k-path for the primitive cell.

The suggested BZ path from SeeK-path was added to the .cell file for the band structure calculation. The same basis set as the DOS calculations was used, with the addition of the 'bs_kpoint_path_spacing' keyword in the .cell file to control the number of calculated points on the band structure. The value of the k-point path spacing chosen for all band structure calculations was 0.05.

The band structure output files were data-scraped using the Python-based Sumo DFT plotting module [44]. By visualising the band structure, the electron energy states for GGA, GGA+U and mGGA calculations can all be compared. Furthermore, the band structure can be plotted alongside the density of states to discover which orbitals contribute the most to each band.

For the density of states, both the total DOS and projected DOS (PDOS) were calculated using the 'spectral_task: dos' keyword in the .param file. The output files were passed through OptaDOS to re-calculate Fermi energy with applied smearing, which leads to more accurate results. Additionally, OptaDOS can apply adaptive smearing to raw DOS data, which results in smoother, more realistic DOS data, but with more retained features of the curve unlike using the standard Gaussian smearing. All DOS calculations analysed in this manner used a smearing width of 1.0. All DOS calculations use a denser spectral k-points grid than the main k-points grid to properly encapsulate all important features of the DOS.

3.2.6 Core-Loss EELS

When gathering EELS data from experiment, the energy loss of the electrons corresponds to certain types of EELS spectra. Low loss EELS experimentally studies that spectrum caused by electrons that have lost energies within the range of less than 50 eV. This region is a powerful tool to study the effects of surface plasmons and excitons to name a few phenomena [45]. Core-loss EELS studies the high energy region greater than 50 eV. This spectrum is caused by the excitation of inner core electrons to the CBM [46]. This is of particular use in revealing the bonding structure and electronic properties of a material.

Low loss EELS can be simulated in CASTEP by using the 'core loss' spectral task, and using the default generated pseudopotentials. This was carried out on the primitive cell of NiO to save time as a supercell is not required for this calculation. Furthermore, core-loss EELS can be simulated in NiO by modifying the pseudopotential generation string for one or more atoms in the cell, either by removing an electron from one of the orbitals or by exciting an electron from one orbital to another. Of focus in this study is the nickel L2,3 edge, caused by the excitation of a 2p electron to the 3d orbital. The edge generated from the atom with the modified pseudopotential can be compared to the spectra of the other atoms in the material that are unmodified, and to that of experiment.

The OptaDOS post-processing tool is capable of applying adaptive broadening in the same manner as DOS calculations, however for EELS data OptaDOS can also apply Gaussian broadening and life-time effects to better reflect experimental data. All EELS and core-loss calculations used a broadening value of 1.0 eV, with no applied Gaussian broadening and life-time effects applied, with a Lorentzian width of 0.5 eV and Lorentzian scale of 0.1. After

post-processing, the calculated EELS edges were compared with an experiment dataset obtained from the EELSdb website, collected by P. L. Potapov *et al* [47][48].

3.3 Results and Discussion

3.3.1 Convergence Tests

Cut-off Energy Convergence Testing

The RSCAN and PBE cut-off energy results obtained similar values for the ground state energy, even though they used different pseudopotentials. Additionally and more importantly they both showed a similar trend in terms of convergence error. The fact that they are both similar enough means that the chosen cut-off energy for all calculations will be transferable for both RSCAN and PBE calculations.

This trend was also true for CuO, with a convergence error that showed some transferrability between RSCAN and PBE results. In addition to this, the convergence error appears to level out at the same points compared to NiO. This is somewhat to be expected due to the atomic similarity between Ni and Cu.

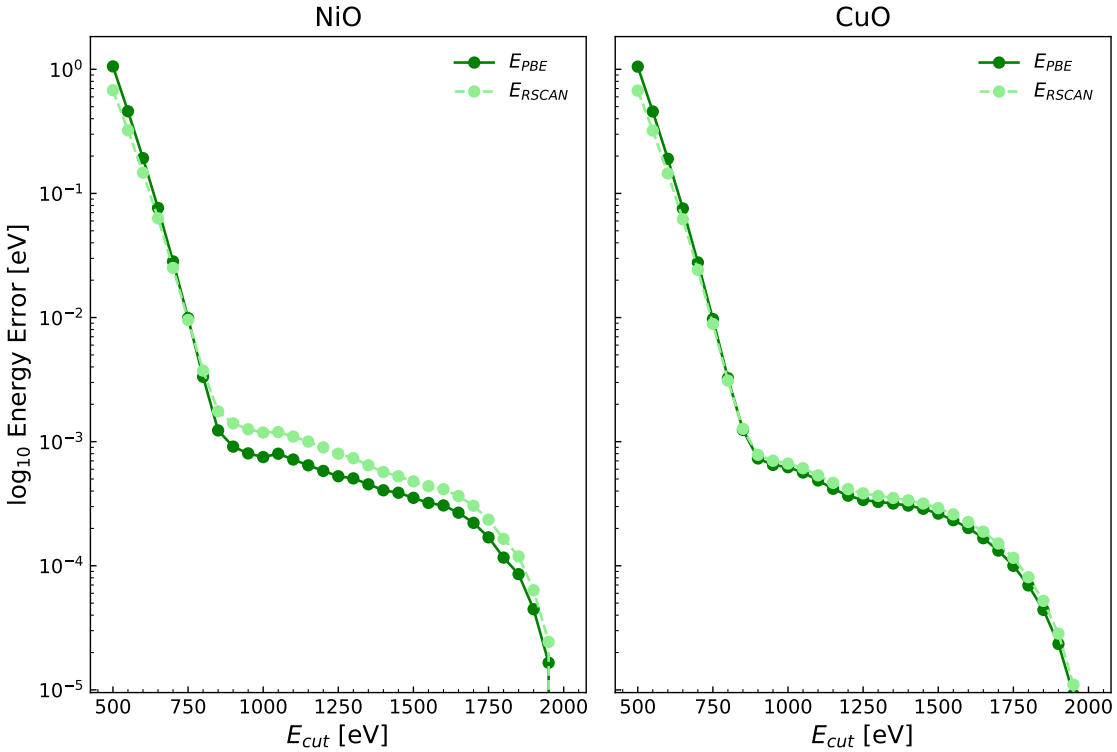

Fig. 3.5 Energy convergence error plotted on a logarithmic scale with increasing cut-off energies. SCF convergence tolerances of 10^{-8} eV and 10^{-3} eVÅ^{-1} for the energy and forces were used respectively.

The convergence results for F_{max} also showed little difference in error between RSCAN and PBE, with RSCAN containing a few anomalous peaks. These results are shown in more detail in figure A.1 within the appendix.

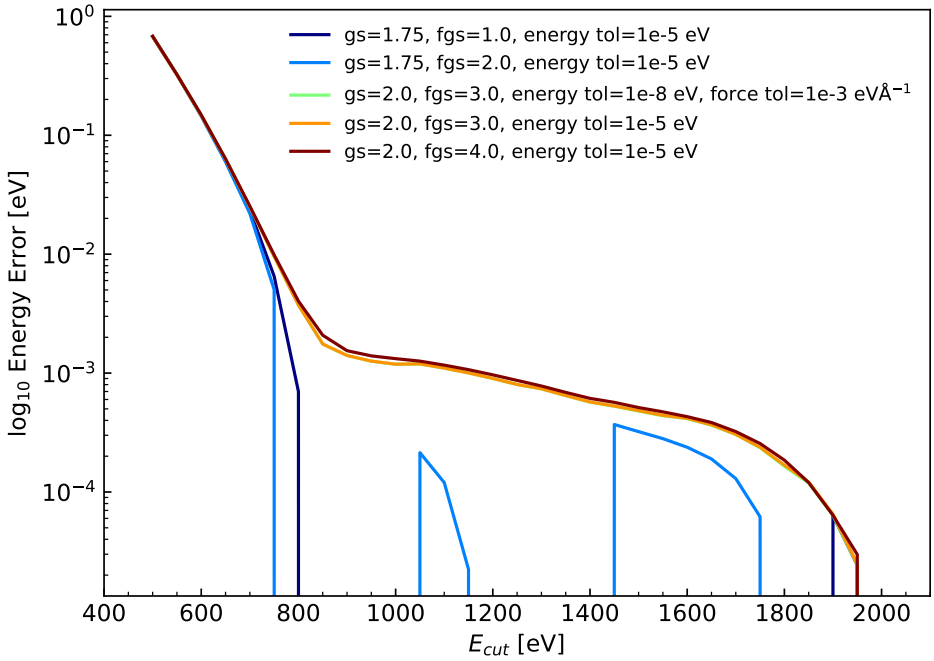

Fig. 3.6 Energy convergence error plotted on a logarithmic scale with increasing cut-off energies, grid scales, and varying energy and force tolerances.

A cut-off energy of 800 eV corresponds to a convergence error of 10^{-3} eV per atom. After this cut-off energy, the change in convergence error drastically reduces up until 1800 eV. The value of 800 eV was chosen based on the fact that it is just at the start of the region of diminishing returns with regards to reducing convergence error vs computational cost.

Using the default grid scale of 1.75 resulted in discontinuities in the log of the convergence error. This alludes to a problem with the sampling grid not being fine enough to accurately calculate the electron densities. Through further testing, this was confirmed by analysing the calculated internal forces in the cell, which showed a drastic increase at certain cut-off energy ranges. This problem is clearly resolved by increasing the grid scale and fine grid scale slightly to better resolve the electron density. It was decided that a grid scale of 2.0 and fine grid scale of 3.0 was enough when paired with the chosen cut-off energy of 800 eV.

In addition to the grid scale, an energy tolerance of 10^{-8} eV and force tolerance of 10^{-3} eVÅ^{-1} was introduced to ensure that the SCF convergence was very finely converged. This had little effect on the energy convergence error, but greatly impacted the force convergence error as shown by figure A.3.

K-point Grid Convergence

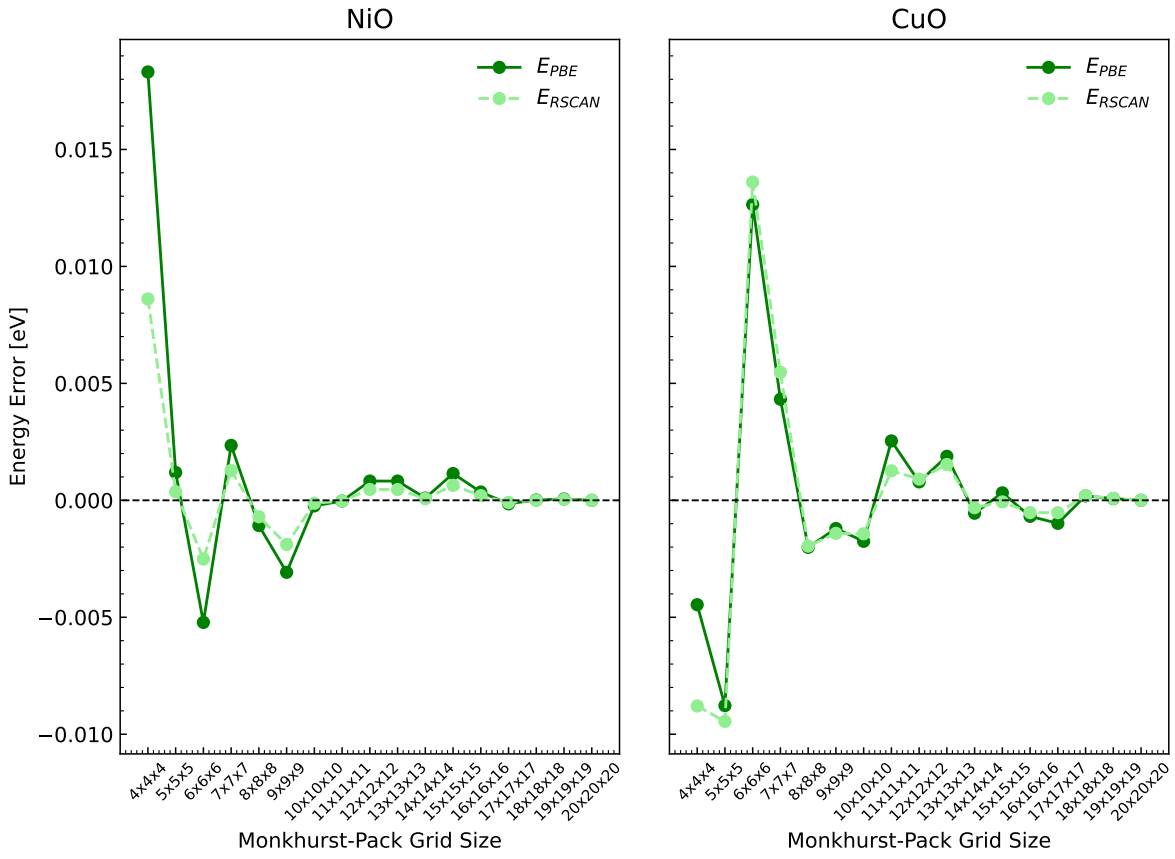

Fig. 3.7 The energy convergence error plotted with increasing k-point grid density.

The energy convergence error exhibits oscillatory behaviour. This is due to the fact that even Monkhorst-Pack grid values sample the centre of the BZ, unlike odd values. This leads to a discrepancy between even and odd grid values which in turn causes oscillatory behaviour when both are plotted on the same axes.

The force error data values are negligible within the applied SCF convergence tolerances. The PBE force error data seems to oscillate with increasing amplitude at higher grid sizes as shown by figure A.2. The fact that this behaviour is not shown when RSCAN is used shows that this problem is inherent to the PBE calculation, and not mGGAs overall.

It was decided that a k-points grid of $12\times12\times12$ would be sufficient for the properties that are being studied going forwards. If phonon calculations were to be carried out, a much denser grid would be needed, with a maximum grid density greater than $20\times20\times20$.

3.3.2 Hubbard U Calculation

The linear response calculation produced an output file that contained the χ_0 and χ^{-1} matrices and the Hubbard U values of 5.62 and 5.58 eV for Ni1 and Ni2 respectively.

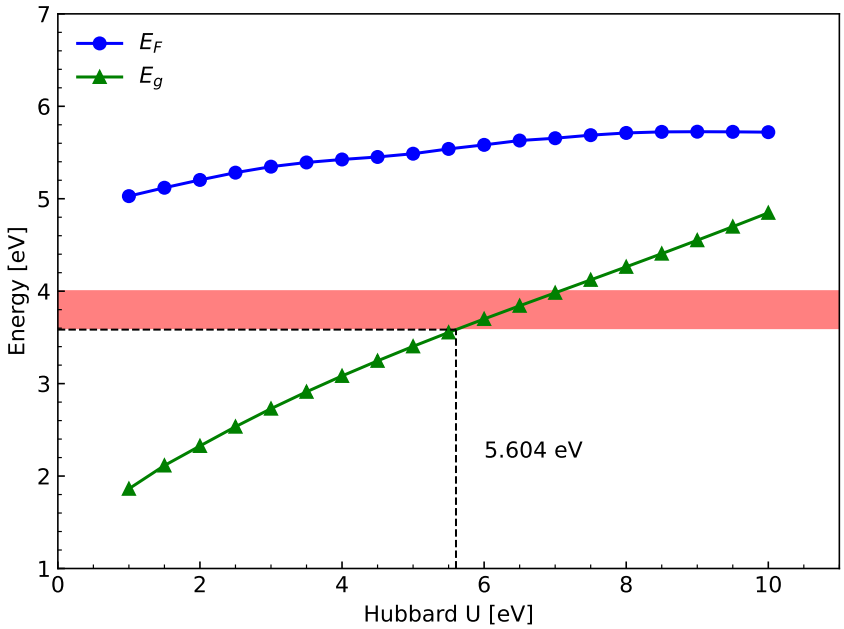

Fig. 3.8 Investigation into how the Hubbard U value defines the Fermi energy, E_F and band gap, E_g. The red highlighted region covers the experimental NiO band gap range of 3.6-4 eV.

The U=5.62 and 5.58 eV obtained from the use of the linear response method for Ni1 and Ni2 respectively was chosen for all PBE+U calculations, resulting in an electronic band gap of 3.58 eV after comparison with the experimental band gap range as a confidence check.

Other studies have found that U=5.5 eV for the Ni 3d orbital is sufficient for calculating the correct band gap [49]. U=5.5 eV corresponded to E_F=6.09 eV and E_g=3.7 eV. The E_F values levelled out after U=6.0 eV and in fact decreased slightly after U=9.5 eV. This trend is noted to be caused by drastically increased localisation due to a sizeable Hubbard U value. This fact is why U values matching that of the lower-end of the band gap range are better at reproducing more accurate band structures.

3.3.3 Primitive Cell Spectral Calculations

Band Structure

The BZ path sampling for the band structure was selected to be the FCC path. This reason for this is that the rhombohedral cell is derived from the FCC structure, and so retains the Fm-3m path spacing. Most experiments and other computational studies also use the FCC path for NiO, and so defaulting to this is also useful for comparison with other data. The CASTEP calculated PBE, PBE+U and RSCAN band gaps were found to be 1.35 eV, 3.58 eV, and 1.68 eV respectively, with the PBE calculation expectedly giving the smaller band gap. Both the PBE and RSCAN band gaps are well below that of the experimental values of 3.6-4 eV, with RSCAN performing slightly better between the two.

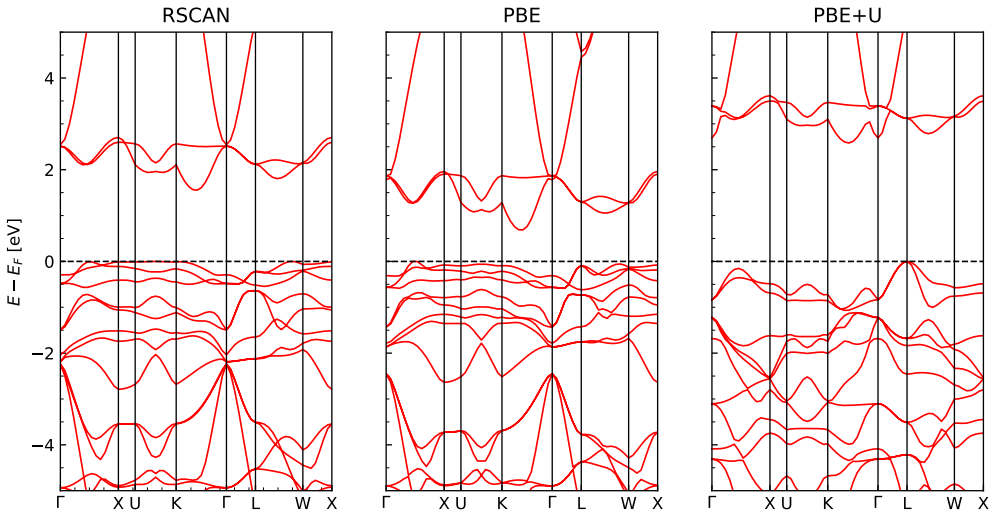

Fig. 3.9 Band structure comparison for NiO with different XC-functionals. E_F is 3.99, 4.99, and 5.44 eV from left to right respectively.

The PBE+U band structure is noticeably different compared to both RSCAN and PBE, which are both very similar to each other. The difference in the band structure by applying a Hubbard U value is a result of the increased localisation of the Ni 3d orbital, which seemingly has reduced the number of VBM states, alongside reducing the flatness of the bands. This indicates that the 3d orbitals are overlapping less with other orbitals as a result of the increased localisation.

Table 3.1 Comparison of CASTEP/OptaDOS calculated values and experiment. For the PBE+U calculations, U=5.604 eV. The experimental Fermi energy of 5.0 eV is a widely accepted value [50].

Method	Fermi Energy (eV)	Band Gap (eV)	Magnetic Moment (μ_B)
PBE	4.87	1.35	1.30
PBE+U	5.55	3.58	1.61
RSCAN	3.21	1.68	1.45
Experiment	5.00	3.70	1.90

Density of States

The RSCAN calculations showed that the majority of the energy states both within the VBM and CBM was formed from Ni 3d states, with O 2p and Ni 2p forming the majority of states at energy values below -3.0 eV with respect to the Fermi level. In contrast, figure 3.10 shows that by applying a U value to the Ni 3d orbitals, all states below the VBM are dominated by the oxygen 2p orbital.

Of particular note is how much lower the DOS energy states are when comparing the two XC-functionals. The cause of this disparity is the increased localisation of the Ni 3d orbitals leading to an alteration of the occupancies.

The local magnetic moment of the Ni atoms is underestimated by between 11-37.5% compared to the experimental value for all XC-functionals tested. This is due to correlation effects, the lack of a discontinuity in the derivative of the XC-functional potential term and the self-interaction error, in the same reason why band gaps are underestimated [51][52].

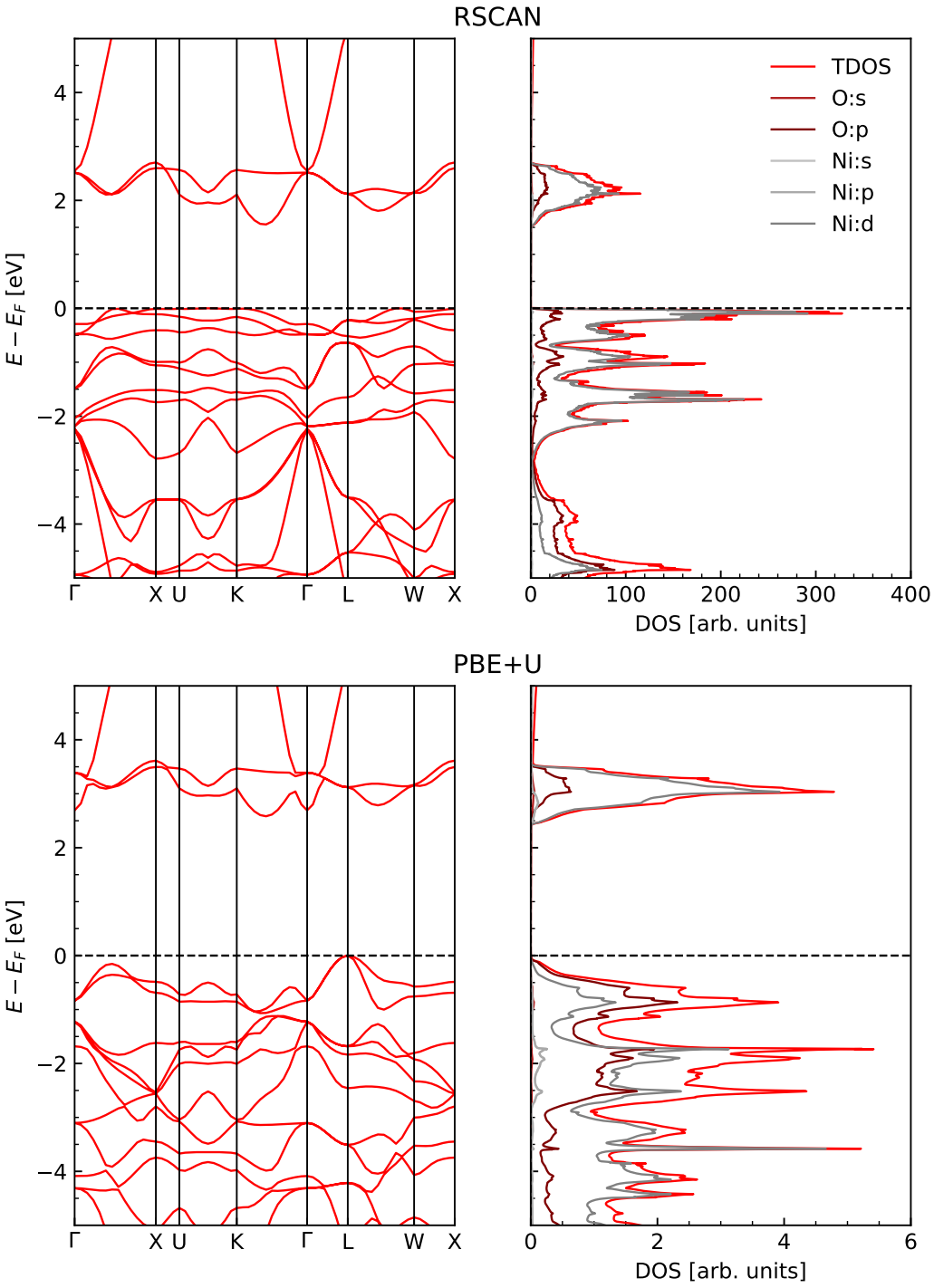

Fig. 3.10 NiO band structure and associated PDOS comparison of the RSCAN and PBE+U results.

3.3.4 Supercell Core-Loss EELS

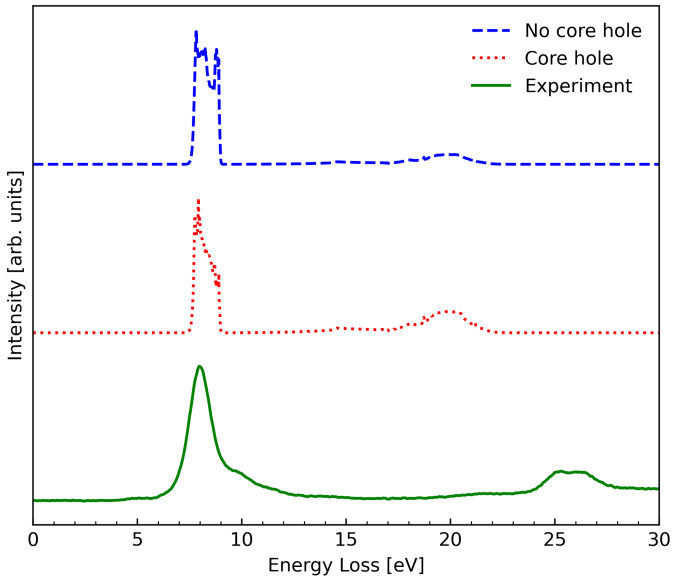

Fig. 3.11 Normalised DFT calculated data sets with and without a core-hole compared with an experimental dataset of the EELS Ni L2,3 transition edge. Experimental data is shifted by 847.40 eV and the DFT data is shifted by the Fermi energy of 3.8555 eV to align the first peak.

The general features of the DFT calculation for both with and without core-holes aligns with that of experiment somewhat. The L3 edge for the core-hole result more closely matches that of experiment, with the graduate levelling off of the second part of the main peak more closely resembling that of experiment. The L2 edge, corresponding to Ni 3d states, is more prominent for the core-loss example.

Table 3.2 Each spectrum type with the ratio of the maximum intensities of the L3 and L2 edges respectively.

Type	I(L3):I(L2)
No core-hole (DFT)	0.073
Core-hole (DFT)	0.157
Experiment	0.327

There's evidently less of a gap between the L2 and L3 edges in the DFT spectra. It is well documented that in standard DFT, any L2,3 transition calculations for TMOs often fall short of accurately fitting the experimental data. This is known to be caused by the lack of multiplet

effects being accounted for, primarily arising from the lack of spin-orbit coupling effects for the TM core 2p elecrons [53].

3.4 Conclusion

The 4 atom NiO rhombohedral cell with its rigorously tested basis set is enough for the creation of supercells which can be used to test the effects of doping. The band structure and DOS with different functionals showed some differences arising from increased localisation, particularly RSCAN/PBE vs PBE+U. The band gap was underestimated as expected and was corrected using the DFT+U method of the use of linear response theory to find the suitable U for the system. The band structure and DOS data showed that the bands at the VBM and CBM are mostly composed of Ni 3d states, alongside O 2p to a smaller degree.

The core-loss EELS simulation of NiO yielded results with RSCAN that still showed the effects of the less-localised d orbitals. The Ni 2p core-hole Ni atom more closely resembled that of experiment, which is expected given the L2,3 edge is a result of the 2p to 3d electron transition.

Chapter 4

NiO Defect Calculations

4.1 Introduction

Defects in materials must be considered to obtain the whole picture of a material's properties. Extrinsic and intrinsic defects all can result in big changes to a materials electronic landscape, and thus its properties. In this chapter, NiO cells containing defects are scrutinised to ascertain as to how its properties will change with added defects. Both vacancies, copper atom substitutional and interstitial defects are all considered and compared with one another. Furthermore, the 10% Cu-doped cell spectral and optical properties are studied.

4.2 Types of Defects

Intrinsic defects are a subclass of substitutional defects, with an atom being removed leaving a vacancy. In NiO, nickel vacancies, V_{Ni} are responsible for making NiO a p-type semiconductor [54]. Without these defects, bulk NiO would remain an insulator and thus be more undesirable in its current applications. In order to understand the most favourable defect type to form given the chemical environment, it's necessary to calculate the defect formation energy, $\Delta H_{D,q}$ [55].

$$\Delta H_{D,q} = \left[E_{D,q} - E_H\right] + q\left(E_V + \Delta E_F\right) + \sum n_Q \left(\mu_Q^0 + \Delta\mu_Q\right) \tag{4.1}$$

$n_Q = +1$ if an atom is being removed, and $= -1$ if an atom is being added. μ_Q is the chemical potential of the species being added or removed. $E_{D,q}$ is the total energy of the defect cell, E_H is the total energy of the pure cell with no defects, E_V is the VBM energy of the defect cell, and ΔE_F is the change in Fermi energy between the defect and pure cells.

4.3 Computational Methodology

4.3.1 Vacancy Cell Creation

The pure NiO supercell was taken and the centre Ni atom was removed to create a vacancy. This cell was then relaxed and the final energy was noted. As Ni was removed from the cell, it was necessary to compute the chemical potential of pure Ni metal. As the unit cell of FCC Ni metal contained 4 atoms, the final energy was divided by four to obtain the chemical potential of 1 Ni atom. The charged vacancies V_{Ni}^{+1}, V_{Ni}^{+2}, V_{O}^{-1}, and V_{O}^{-2} were not considered. This is due to the fact that the rhombohedral supercell is rather long and thin, and thus the coulomb repulsion energy between the periodic vacancies would be too large to claim accurate results, especially for the doubly charged defects. The Coulomb repulsion energies were calculated and are shown in figure A.6 within the appendix.

Using equation 4.1, the defect formation energy depending on the chemical potential limit (defined by the $\mu_O^0 + \Delta\mu_O$ term) can be calculated. To investigate this, the chemical potential of Ni, Cu, and O was calculated using CASTEP, using the same cutoff energy of 800 eV, but with a $20\times20\times20$ k-point grid for the metallic ions and $1\times1\times1$ gamma point sampling for the O_2 molecule. In the oxygen-rich limit, the computed μ_O was used to determine μ_{Ni}, and conversely in the oxygen-poor limit the computed μ_{Ni} is used to calculate the μ_O.

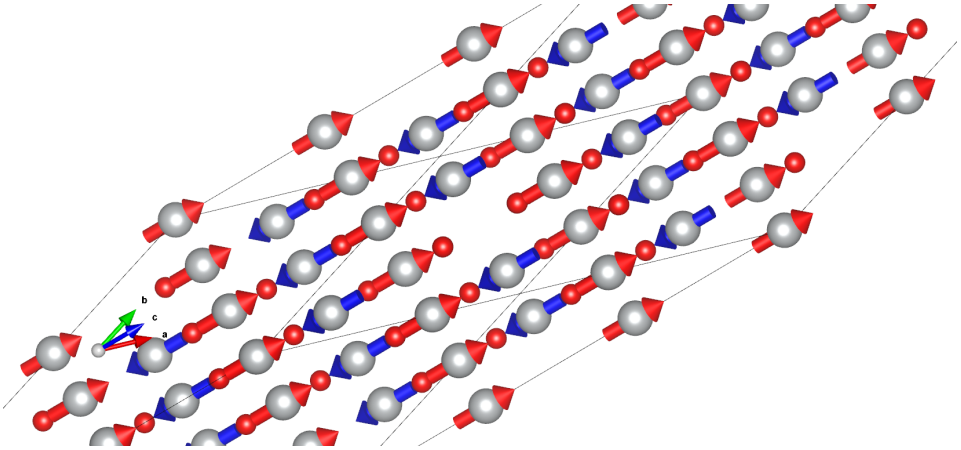

Fig. 4.1 Ni vacancy in the centre of the cell along the spin down [111] plane of Ni (silver)

4.3.2 Cu-doping Cell Creation

1 Cu Atom Systems

Alongside intrinsic defects are extrinsic defects. These defects involve the incorporation of atom(s) from another species into a crystal structure on established atomic sites. This occurs by

the dopants displacing an atom from the original crystal. This differs from intrinsic defects by dopant atoms being interstitially incorporated in the space in between atoms, or there being an atom removed from the structure, forming a vacancy.

The act of doping a material extrinsically or interstitially can drastically change a material's properties. The majority of calculations involving Cu-doping of NiO in this project involved replacing Ni and O atoms in the structure with Cu, with the Cu atoms acting as extrinsic point defects. Extrinsic defect formation energy can also be calculated in the same manner as intrinsic defects, with the chemical potential of Cu now coming into play.

The 3x3x3 NiO supercell was altered to include a Cu atom at the centre of the cell, replacing the Ni atom to form a neutral Cu_{Ni} defect. This corresponded to a doping concentration of approximately 2%. Similarly, an oxygen atom adjacent to the Ni atom at the centre of the cell was removed to form neutral Cu_O, and finally a neutral interstitial Cu atom was added into the structure in the $0.48\bar{3}$, $0.48\bar{3}$, $0.48\bar{3}$ fractional coordinate positions to form Cu_i. This defect was also placed close to the centre of the cell.

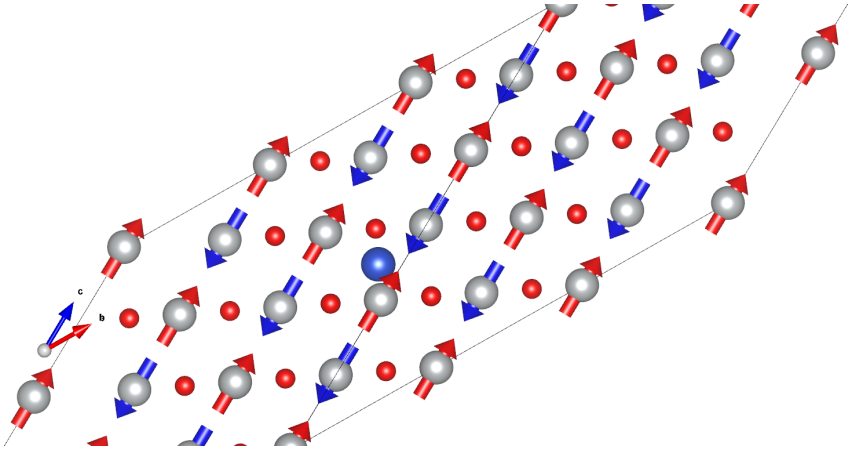

Fig. 4.2 Interstitial Cu atom (blue) amongst the spin up and down [111] planes of Ni (silver)

2+ Cu Atom Systems

To investigate how the energetics and electronic properties may vary for increasing numbers of Cu atoms, it was decided that a quick test would be to investigate the 2 Cu atom system. This involved the creation of 3 supercells, each with 1 Cu atom in the centre. The first cell had an additional Cu atom placed at the (0, 0, 0) coordinates, the second one with the two Cu atoms being nearest neighbours, and then the final one with a Cu atom approximately in between these two extremes. These cells corresponded to a doping concentration of approximately 4%. These cells would then be relaxed using the same basis set as the other calculations, with further DOS calculations also being carried out using these cells.

An investigation was also carried out to determine whether the Cu atoms prefer to align themselves along the [111] plane or on the next along, oppositely spin-polarised [111] plane.

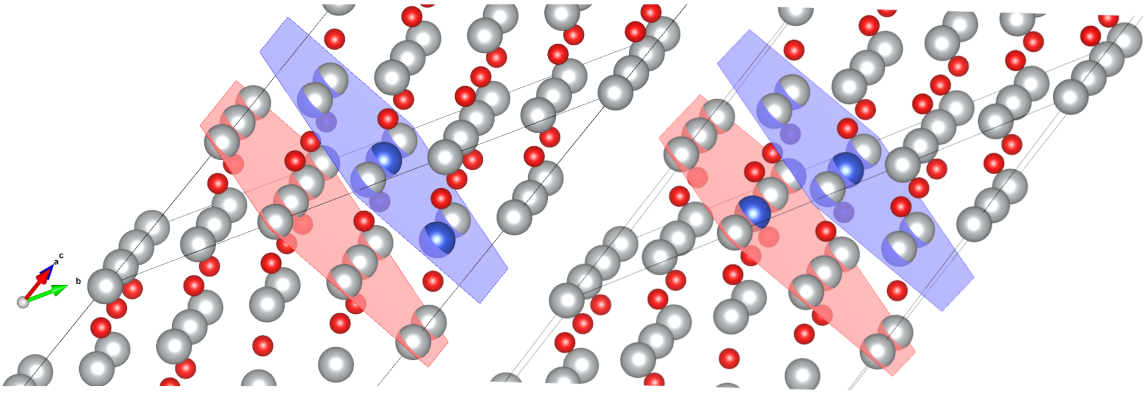

Fig. 4.3 Two different close proximity configurations of the 2 Cu_{Ni} defect cell. The red [111] plane represents the spin up plane, with the blue [111] plane representing the spin down.

To really push the limits of doping, the 10% doped case was also investigated. This involved substitutionally placing 6 Cu atoms randomly on Ni sites. A cutoff energy of 800 eV was used, with a k-points grid of 2×2×2 being used to save computational expense and thus aid the SCF convergence. A 1600 eV density mixing cutoff energy was also applied to this end.

4.3.3 Spectral Calculations

Of particular interest is how the incorporation of Cu into NiO affects the electronic properties of the material. To study this, the band structure and DOS was calculated for each of the different 1 Cu atom defects and compared. A cut-off energy of 800 eV and k-points/spectral k-points grid of 4x4x4 and 8x8x8 4×4×4 and 8×8×8 respectively was used for all DOS calculations. Additionally, the spin behaviour and energetics of multiple doping percentages of Cu atoms was analysed by performing band structure and DOS calculations, with a focus on how the positioning of the Cu atoms changes the electronic properties.

4.3.4 Optical Calculations

The optical calculations were largely carried out using the same method as the NiO 3×3×3 supercell calculations. The main difference was that the cell being used for the defect cell contained 10% Cu atoms replacing the Ni atoms. 25% of the optical band gap of the bulk NiO was used as the scissor operator in both cases to allow for the comparison between the two materials. To align the theoretical results with that of experiment, OptaDOS allows the use

of an arbitrary spectral-shift value called the scissor operator. The scissor operator value is determined by taking the difference between the true experimental band gap and that calculated by a DOS calculation. As numerous studies have shown a band gap value between 3.6-4.0 eV, a value of 3.6 eV was chosen as the true value. Previous DOS calculations of bulk NiO using PBE produced a band gap value of approximately 1.3 eV, which resulted in a scissor operator value of 2.25 eV. The same scissor operator was applied for both the undoped and doped cases, for the sake of comparison.

4.3.5 Electron Microscopy Simulations

Additional calculations were carried out involving the relaxation of Cu-doped NiO cells and the simulation of electron microscopy images of materials constructed from these cells. As these results were of little impact to the main body of work in this study, they are discussed in more detail within appendix B.

4.4 Results and Discussion

4.4.1 V_{Ni} and V_O Defect Formation Energies

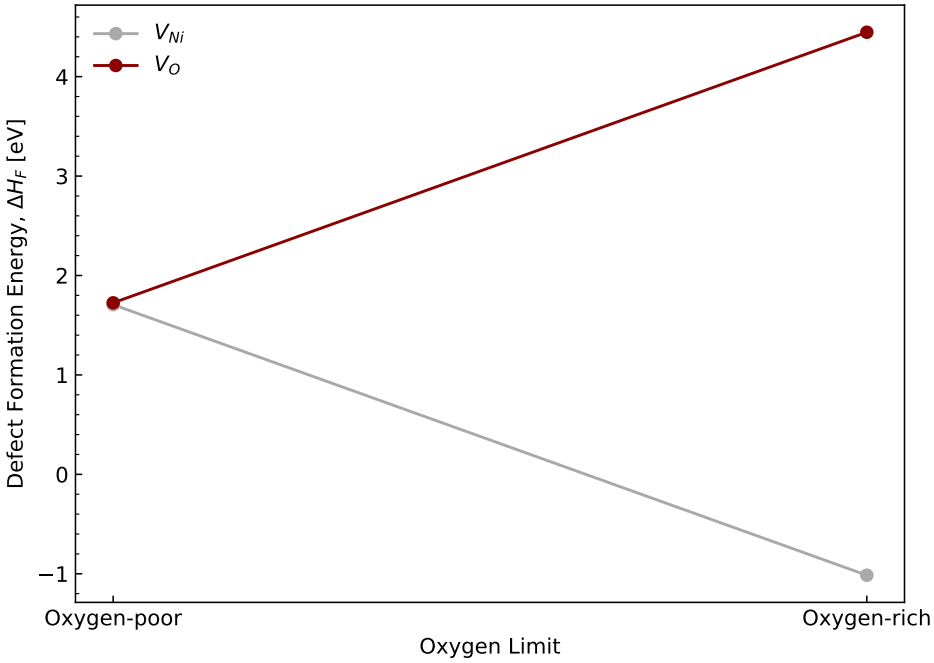

Fig. 4.4 Both neutral vacancy defect formation energies in the oxygen limit. The computed μ_{Ni} and the μ_{Ni} given by the computed μ_O are used in the oxygen-poor and rich limits respectively.

Given oxygen-rich conditions, nickel vacancies are the most favourable to form with a considerable margin compared to oxygen vacancies. This is expected from experimental studies of NiO, showing that V_{Ni} is the dominant form of vacancy, and in fact contributes to making bulk NiO a p-type semiconductor [56]. Oxygen-poor conditions show that it's equally favourable for both types of vacancy to form.

4.4.2 Spectral Calculations with Vacancies

V_{Ni} DOS

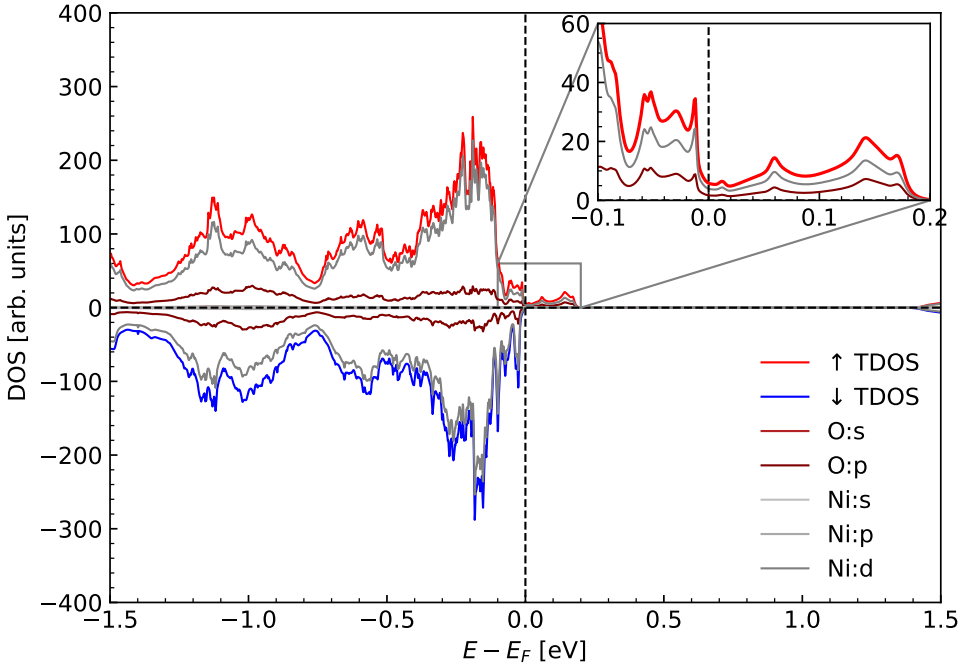

Fig. 4.5 V_{Ni} PDOS centred at the Fermi energy, with E_F=3.12 eV.

The PDOS calculation revealed that the highest energy orbital angular momentum states formed spin-polarised energy states above the Fermi level, therefore the band gap of the material narrows as a consequence. Additionally, this state above the Fermi level suggests that the material is a p-type semiconductor, which is a key property of bulk NiO.

V_O DOS

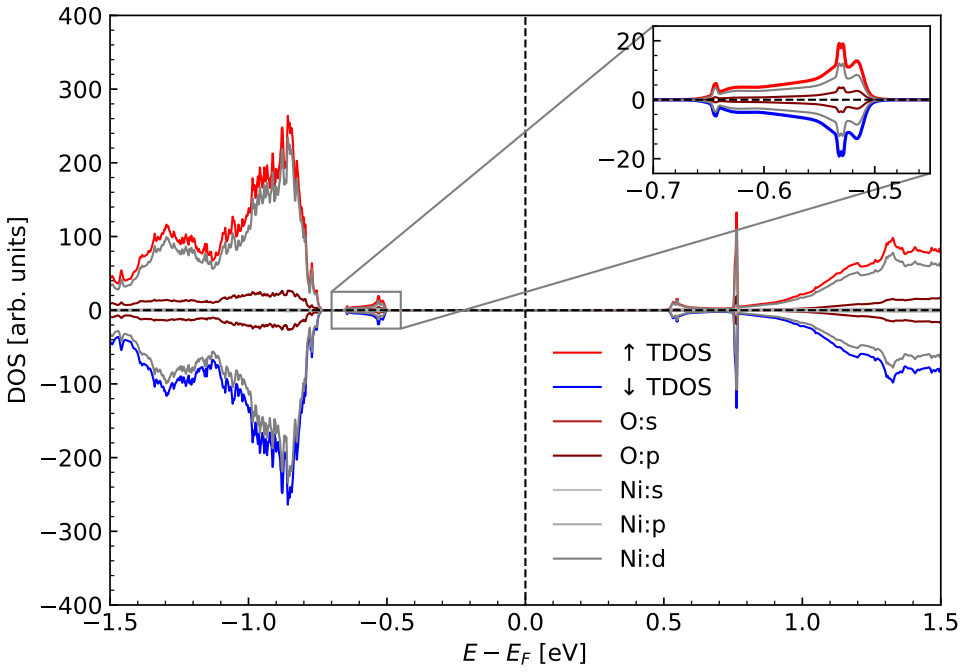

Fig. 4.6 V_O PDOS centred at the Fermi energy with E_F=3.89 eV.

The V_O case showed the greatest disparity compared with the other two, with states forming above and below the VBM and CBM respectively. This very much narrows the band gap and thus has important consequences for the electronic properties of the material. This is reasonable considering experiment has shown that NiO with abundant oxygen vacancies has improved conductivity and increased charge transfer rates [57]. Additionally, there is a large peak at around 0.75 eV in both the spin up and down channels. This peak largely consists of Ni 3d energy states. Sharp peaks such as this have been reported to be caused by flat bands, thus implying that there is a low amount of orbital overlapping for the Ni 3d energy states [58].

4.4.3 1 Cu Atom Defect Formation Energies

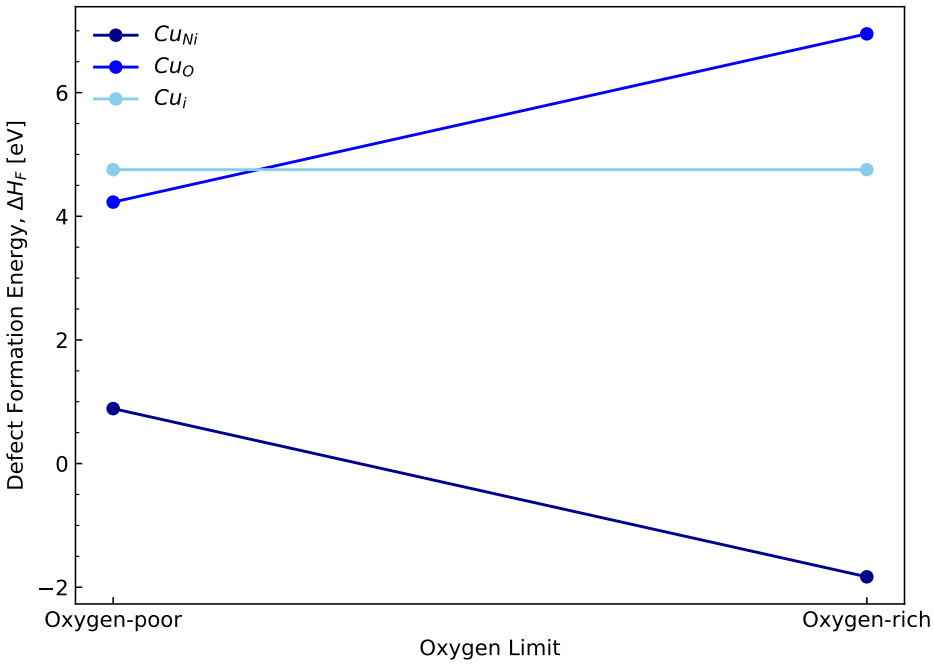

Fig. 4.7 Defect formation energies of Cu atom in NiO in the oxygen limit. The computed μ_{Cu} is kept constant, with the computed μ_{Ni} and the μ_{Ni} given by the computed μ_O being used in the oxygen-poor and rich limits respectively.

A similar trend was observed for the Cu doping defect formation energies, with Cu_{Ni} being by far the most favourable to form. Logically this is to be expected, as Cu and Ni are both similar in atomic structure. Both elements differ from one another by a proton and an electron and thus Cu atoms should tend to fill in any Ni vacancies that form. Following this logic, this would explain why Cu_O was a lot less favourable to form, as Cu and O atoms are in a completely different group in the periodic table, and so have vastly different chemical properties. This fact explains the large difference in defect formation energy for Cu_{Ni} and Cu_O compared to V_{Ni} and V_O, regardless of the oxygen limit.

4.4.4 1 Cu Atom Spectral Calculations

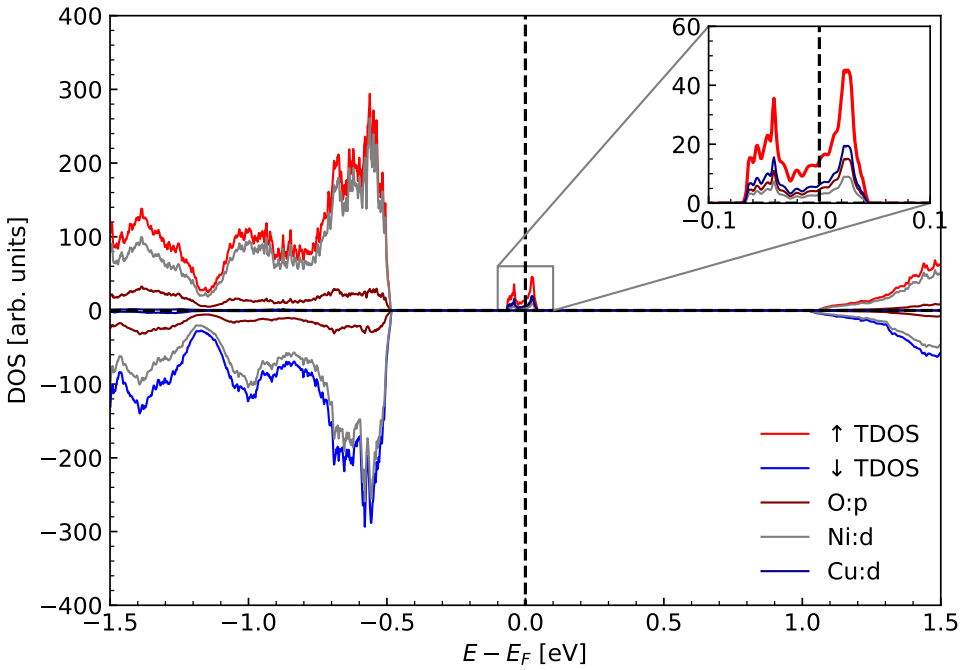

Fig. 4.8 Cu_{Ni} PDOS centred at the Fermi level, with E_F=3.68 eV.

The addition of the copper atom clearly introduces energy states at the Fermi level. The peak at the Fermi level shown by figure 4.8 is composed of the highest energy level orbitals for each species, Ni 3d, Cu 3d, and O 2p. This phenomena has been documented with other dopants for NiO, such as with the group one metals.

Comparison of Cu Atom defect types

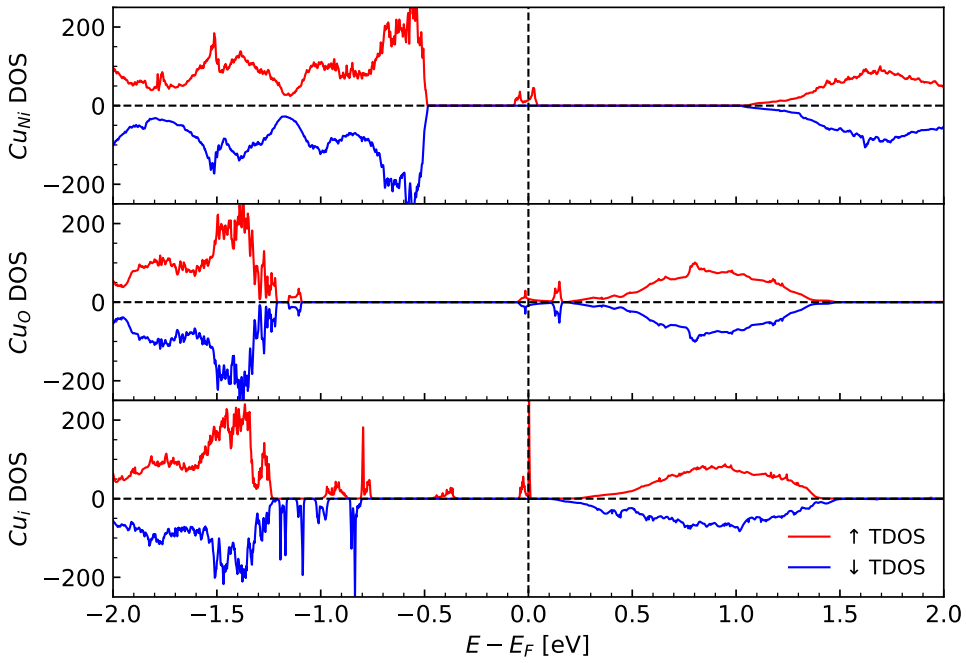

Fig. 4.9 TDOS comparison of all copper defect types. E_F for Cu_{Ni}, Cu_O, and Cu_i is 3.68, 4.51, and 4.58 eV respectively.

It is visible from figure 4.9 that many more states appear in the band gap in the Cu_O case compared to Cu_{Ni}. This is simply because the dopant Cu atom contains more electrons than the replaced O atom, and thus the Cu donates more electron energy states to the supercell, leading to increased n-type behaviour. This trend is extended even more when looking at the Cu_i case, as in this system only electrons are added, with no atoms being removed from the system. A result of this is that there are many more states forming within the band gap, all of which are spin-polarised.

In the Cu_O case, the creation of spin-symmetric energy states is the same as in the V_O case, however there is a reduction in the number of states and also a lack of any flat bands. This would suggest that the addition of the copper atom on the oxygen site has reduced the localisation of the Ni 3d orbitals. Additionally, the position of the Fermi level being so close to the CBM has eliminated the band gap, and thus implies metallic behaviour.

Cu_i DOS

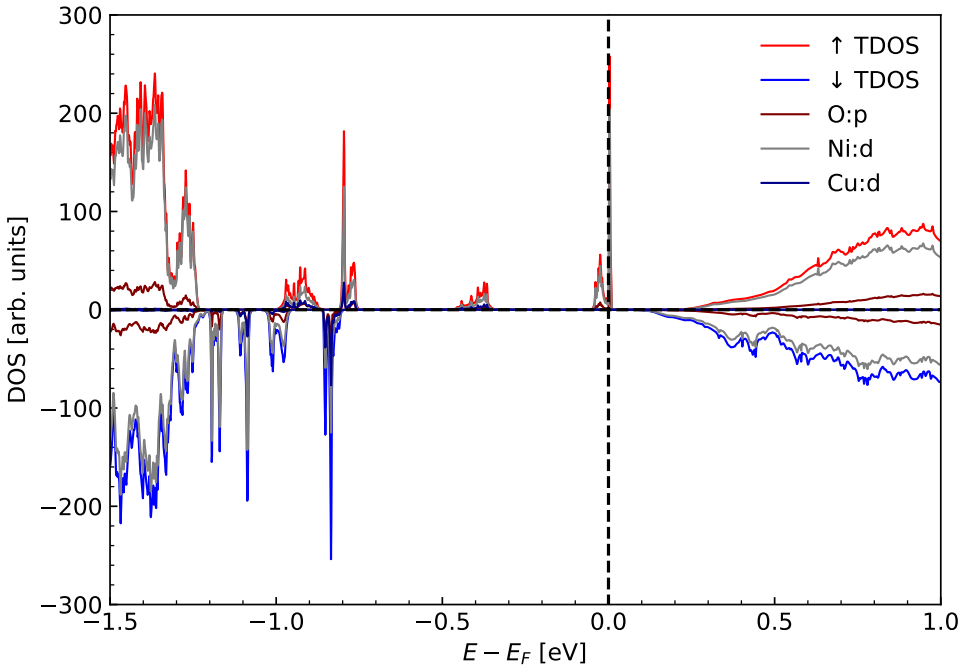

Fig. 4.10 Cu_i PDOS centred at the Fermi level, with E_F=4.58 eV.

Analysis of the composition of the states within the band gap show a mix of dominant projected states. The states are composed of a majority of Ni 3d states, followed by an even amount of Cu 3d and O 2p states. The fact that the Ni 3d states seem to dominate the DOS suggests that the inclusion of the Cu atom has a profound effect on the neighbouring Ni atoms. The states introduced by the Cu atom are a smaller factor in the actual composition of the DOS. There are multiple sharp peaks on and below E_F, which is a typical sign of flat bands. The PDOS decomposition in figure 4.10 shows that these flat bands are dominated by Ni 3d orbitals, with Cu 3d states forming well below the Fermi level. This result would suggest that the interstitial defect is pushing other atoms away, distorting the crystal lattice and resulting in increased overlapping of Ni 3d orbitals. Furthermore, E_F is located very close to the CBM, and thus only a small amount of energy would be required to promote an electron at E_F to the CBM. Therefore, this material has mostly lost its semiconducting properties and has become more metallic.

4.4.5 2 Cu Atoms

The two Cu atom cell setup was created from the one Cu atom supercell, with additional Cu atoms being placed next to the original Cu atom separated by an oxygen atom. This arrangement effectively created a small cluster of CuO within the NiO crystal.

Cu Atom Positional Differences

Table 4.1 Final ground state energy of three cells with the two copper atoms separated by varying distances. ΔE is the difference in the final energy between the most stable configuration and all others.

Distance Apart (Å)	Final Energy per Atom (eV)	ΔE (meV)	Int. Spin Density $\left(\frac{\hbar}{2}\right)$
2.98	-920.768302	0.00	2.00
2.97	-920.767656	69.8	1.29×10^{-4}
7.30	-920.767857	48.1	2.00
21.9	-920.767641	71.4	2.18×10^{-4}

The energy difference between the Cu atom being placed as close and as far away as possible came to 71.4 meV. This suggests that the closer the Cu atoms are together, the lower the ground state energy. Therefore, there appears to be some merit to the claim that TMO dopant atoms tend to 'stick together' and eventually precipitate out in metallic form [59]. Of further note is that the intermediate configuration leads to differences that are approximately half that of the close-far example. This would suggest an almost linear scaling as to the energy difference depending on the proximity of the two Cu atoms to one another.

Additionally, it was found that when the Cu atoms were moved from being nearest neighbours to nearest neighbours +1, the energy difference between the two systems was 69.8 meV This shows that it's more favourable for the two Cu atoms to fill Ni sites on the same [111] plane. Further to this, the Cu atoms seem to gain spin to match that of their Ni neighbours in terms of polarity on the [111] plane. The integrated spin density of the most stable cell was $2.00\frac{\hbar}{2}$, compared to the alternate configuration giving a value of $1.29\times10^{-4}\frac{\hbar}{2}$.

The distance between the Cu atoms in the most stable configuration is 2.98 Å, whereas the less stable configuration has them slightly closer together at 2.97 Å.

2 Cu atom DOS

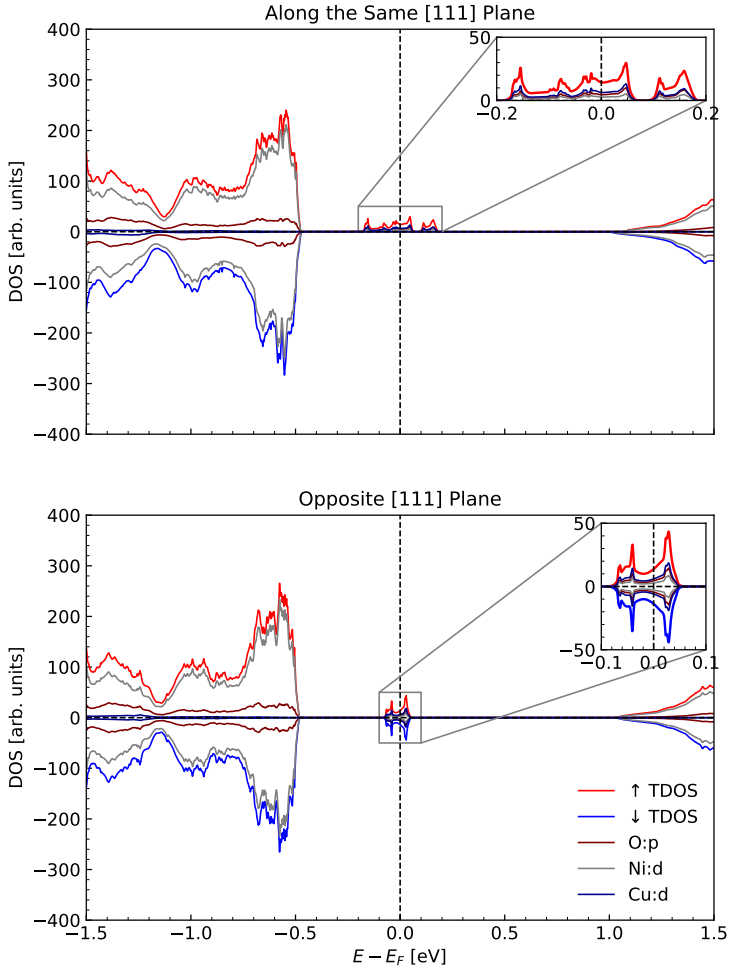

Fig. 4.11 The first plot is that of the two Cu atoms being aligned on the same [111] plane, with the lower plot being the case of the two Cu atoms being on opposite [111] planes. E_F =3.68 and 3.69 eV for the first and second plot respectively.

The DOS results for the two Cu atoms being aligned along the same [111] plane show that there is a widening of the band gap states compared to that of the one Cu atom shown in figure 4.8. On the other hand, the case where they are aligned in opposite [111] planes results in a smaller spin-symmetric gap state forming. The fact that the first configuration is more stable suggests that in doping, the Cu atoms have a clear preference for clustering together and annihilating the band gap with widened energy states over retaining the cell spin symmetry.

4.4.6 10% Doped Supercells

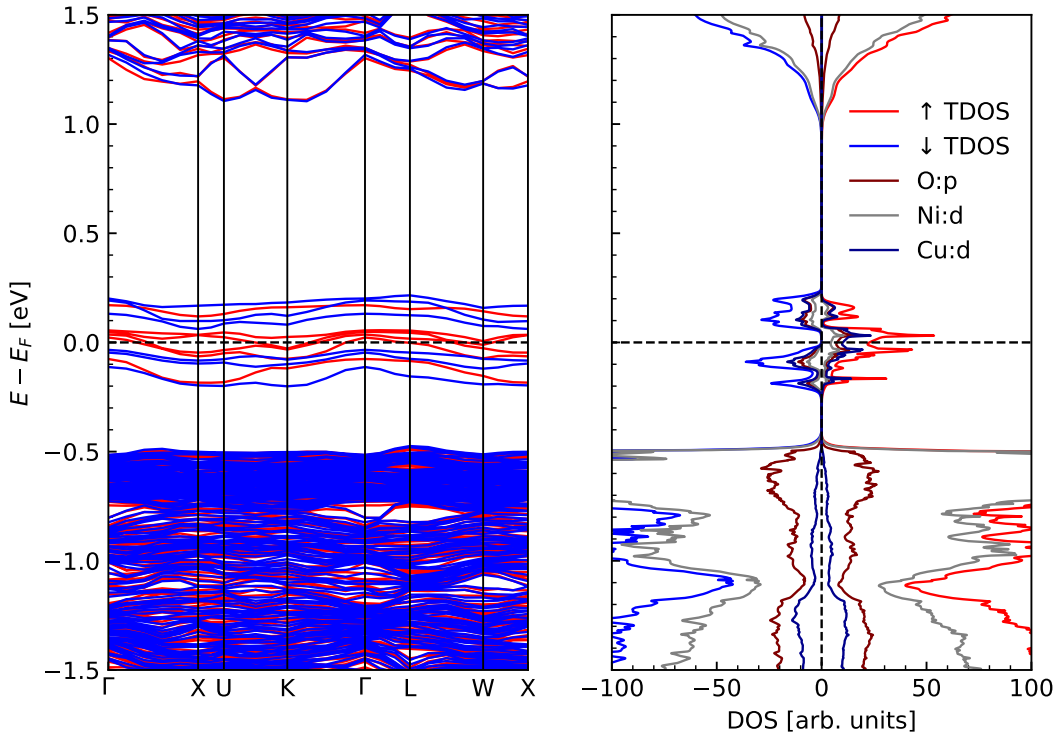

Fig. 4.12 The bands and corresponding DOS states aligned show which orbitals contribute the most to the bands within the band gap. 10% Cu-doped NiO band structure and corresponding PDOS using only Cu_{Ni} sites.

E_F=4.60 eV.

The O 2p orbital states seem to form the most bands in the VBM, with similar amounts of Ni 3d and Cu 3d orbital states. At the Fermi-level of 4.60 eV, the only available states are all spin up. Above and below the Fermi-level there exists a greater amount of spin down states. The significance of this is that all electrons that move to the Fermi-level within the gap state must all be spin up in order to do so. This spin-polarisation is supported by the fact that the integrated spin density is $0.104\frac{\hbar}{2}$, which would suggest that the material is slightly ferromagnetic, with more spin up electrons than down.

Investigating the .castep file reveals that three of the Cu atoms have an overall positive magnetic moment, with the other three having a negative magnetic moment. The magnitude of this magnetic moment varies between 0.37-0.39μ_B. The Ni atoms all have a smaller range of magnitudes, going from 1.58-1.60μ_B. This would suggest that the Cu atoms are having

the greatest impact on the increased spin-polarisation of the material instead of the Ni atoms contributing the most from being disrupted by the Cu atoms gaining a net magnetic moment.

Optical Calculations

Comparing the dielectric constant calculation for the bulk NiO cell and that of the 10% doped cell in figure 4.13, when no scissor operator is applied, for the Cu-doped case there is an increase in absorption between 0-1.2 eV, which places this firmly within the visible light spectrum. There appears to be a decrease in the absorbance of blue light to UV however, with the Cu-doped peak showing more broadening.

When a scissor operator of 2.25 eV is applied, the data shifts to much more realistic values. The peaks are blue-shifted by approximately 2 eV and the amplitude of all of the peaks are reduced.

The real component of the dielectric constant of the Cu-doped NiO remains approximately at 3.59 up until 3 eV, which leads to very gradual increase in both the real and imaginary component, which is negligible up until this point. This trend is similar for bulk NiO, however there is less noise and the imaginary component remains negligible up until 3.5 eV. The significance of this is that the imaginary component of the dielectric function determines the loss in the material, which when looking at the loss function plot in figure 4.13 specifically, it is clear that there is an increase in loss in the Cu-doped material, which gets slightly worse towards the violet and low energy UV part of the electromagnetic spectrum. Furthermore, photons of energy in the middle UV range of 4-6 eV shows a decrease in their absorbance into the material. Figure 4.13 also shows that there is a clear decrease in loss and additional narrowing of the definitive peak in the loss function in the Cu-doped case within the middle UV range. This suggests that doping the material with Cu has improved the potential efficiency of the material, with more photons being absorbed by the material and able to excite the electrons and produce electron-hole pairs.

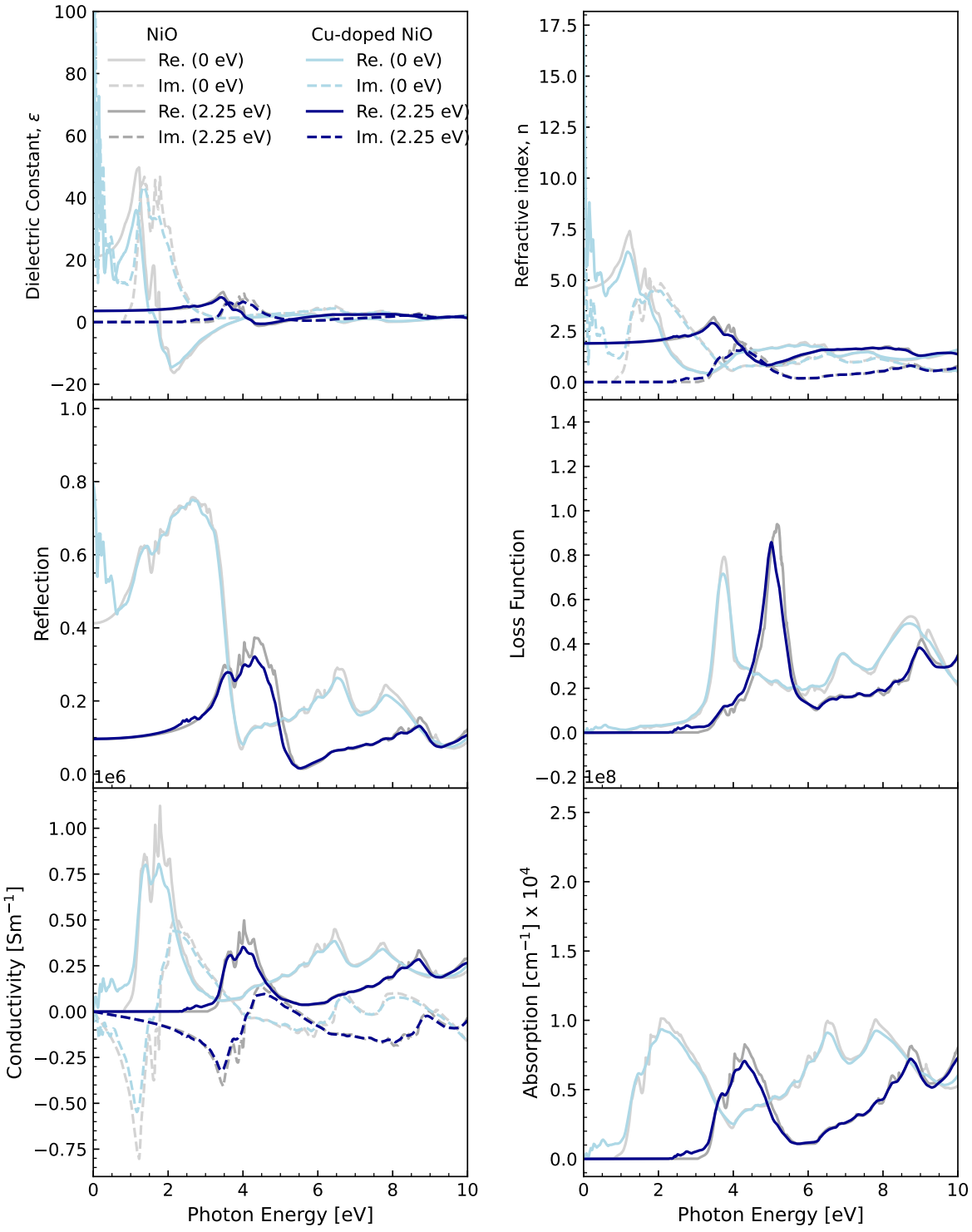

Fig. 4.13 Optics data for the pure NiO and Cu-doped NiO supercells. Bulk NiO data is shown in grey, with the 10% Cu-doped NiO data being shown in blue. The darker colours show the data with the applied scissor operator of 2.25 eV. The real component of the data is shown with a solid line, and the imaginary component with a dashed line.

4.5 Conclusion

The introduction of Cu atoms into NiO showed preferences in terms of their defect type, with Cu_{Ni} being the most likely to form and Cu_O being the least likely defect. This behaviour is in line with the previous results of the vacancy formation energies, showing that Cu atoms are more inclined to fill Ni vacancies and displace Ni atoms where possible.

The Cu_{Ni} defect showed more p-type behaviour when compared to Cu_O and Cu_i showing strong n-type behaviour. Therefore, when doping NiO with Cu, one needs to ensure that the conditions of the chemical environment are as favourable as possible for what electronic behaviour is needed.

The analysis of different cells containing two Cu_{Ni} defects showed that the system of the lowest ground state energy is that of the Cu atoms arranging themselves along the same [111] plane. The implications of this are that the dopants prefer to be as close together as possible, even should the AFM nature of the host cell be disrupted.

The band structure and DOS of the different defects all exhibited the creation of extra energy states from the Cu 3d orbitals hybridising with that of the O 2p. Furthermore, by introducing a large number of Cu atoms into the supercell the AFM nature of NiO is largely disrupted, with large amounts of spin-polarised energy states forming within the band gap.

Optically, the doped cell showed a minor but discernible increase in the absorption of visible light photons compared to that of pure NiO. This is of great importance if Cu-doped NiO is to be used in any applications that depends upon its interaction with visible and UV radiation.

Chapter 5

Convex Hull Calculations

5.1 Introduction

As shown by figure 4.7, Cu atoms prefer to replace Ni atoms in the crystal lattice. To further understand why this occurs and also if there are any more exotic structures that are possible when incorporating Cu into NiO, a ternary convex hull calculation can be performed.

Convex hulls are often used in condensed matter theory for random structure searching, with hundreds, if not thousands of randomly generated cells being relaxed and compared to well known, experimentally observed, stable compounds which form the 'hull'. Multiple species can be added to a convex hull, with 3 species being used in this study. By visualising the formation energies of compounds above and on the hull, it's possible to gain insight into the stability of the generated compounds, alongside structural properties such as symmetries, space groups and lattice constant values to name a few [60].

5.2 Computational Methodology

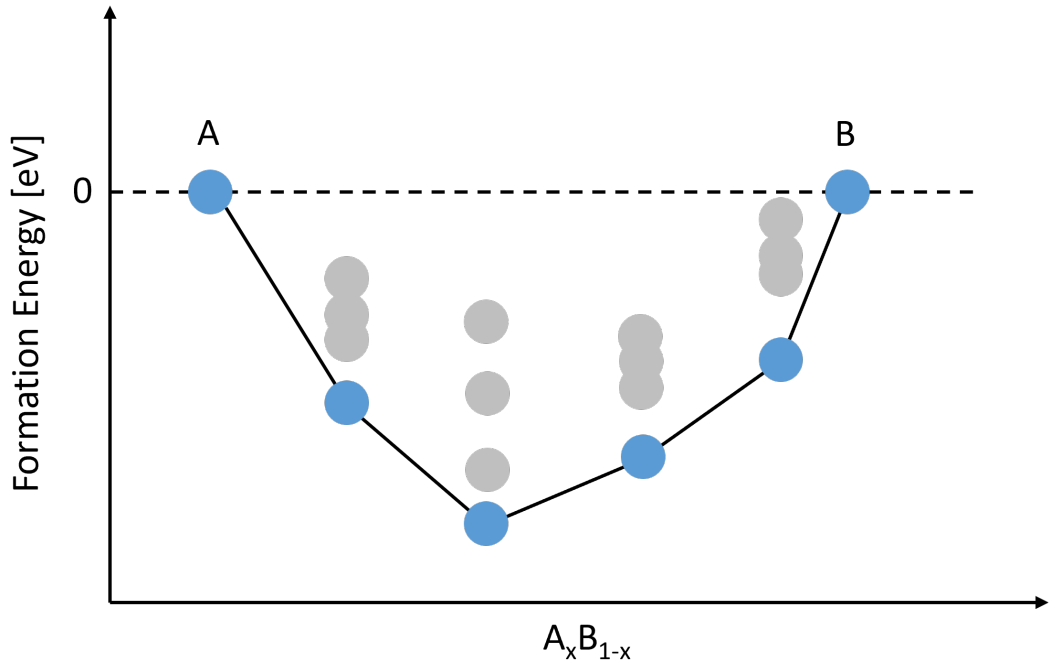

Fig. 5.1 Formation energy of two stable, different species, A and B with all predicted stable compounds of A and B in blue. All unstable compounds are included above the hull in grey.

5.2.1 2D Convex Hull for Ni-Cu-O

To investigate the phases within Ni-Cu-O, a number of structures obtained from the creation of a rough 2D ternary hull from MaterialsProject.org was obtained. All .cif files obtained in this way were converted to .cell files using the 'cif2cell' tool bundled with CASTEP. Suitable cells containing just one species were obtained for use as chemical potential files for the extremities. Additionally, the *ab initio* random structure searching program (AIRSS) was employed to randomly generate structures with varying ratios of Ni, Cu and O [61].

A high-throughput geometry optimisation calculation was carried out using the 'fine' basis set, 0.05 k-point grid spacing and the 'QC5' ultra-soft pseudopotential library. Furthermore, spin effects were not considered for this study. Any .castep files of successfully relaxed structures was data-scraped and plotted using the Matador-db chemical analysis Python program [62].

5.3 Results and Discussion

5.3.1 2D Ni-Cu-O Random Structure Searching

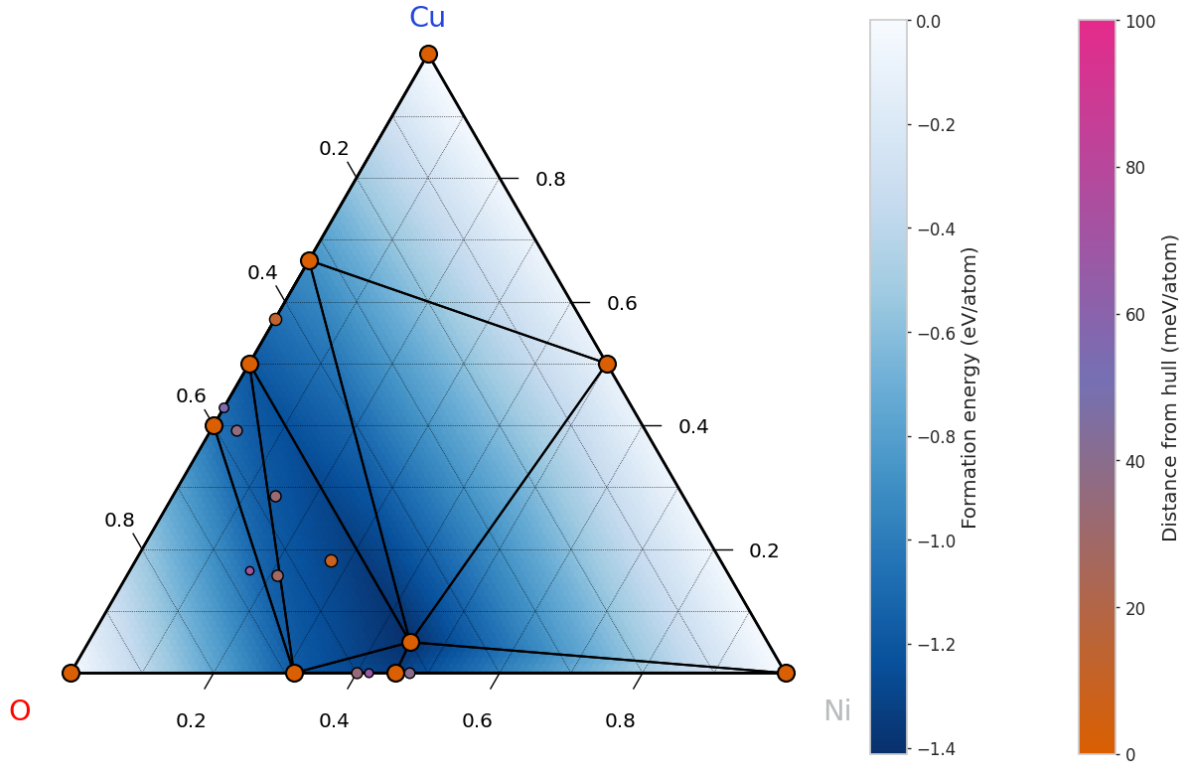

Fig. 5.2 Stable structures on the hull with added phase lines forming the hull surface. The formation energy distribution is plotted in the background as a visual aid for analysing metastable/stable structures. Only structures less than 0.1 eV above the hull are shown.

Most stable phases of the copper and nickel oxides were found, with the exception of FCC NiO. One possible explanation for this is the lack of spin states on the Ni atoms for these calculations. One predicted stable state containing all three species was found, being Ni_9CuO_{10}. From inspection, it is visible that the crystal lattice is arranged in an FCC-like configuration. No other structures containing all three species were predicted stable. This implies that, subject to further testing, any structures that contain all three species are most stable when arranged in an FCC crystal lattice, similar to that of the ground state configuration of NiO.

There is also a trend of structures being closer to the hull the nearer they are to the Ni_9CuO_{10} structure. This is expected from the formation energies being lowest within this region. This would also suggest that structures with a ratio of TM to oxygen of 1:1 is more stable. This is in agreement with current knowledge of doping NiO, with dopants tending to fill the Ni sites over the O sites.

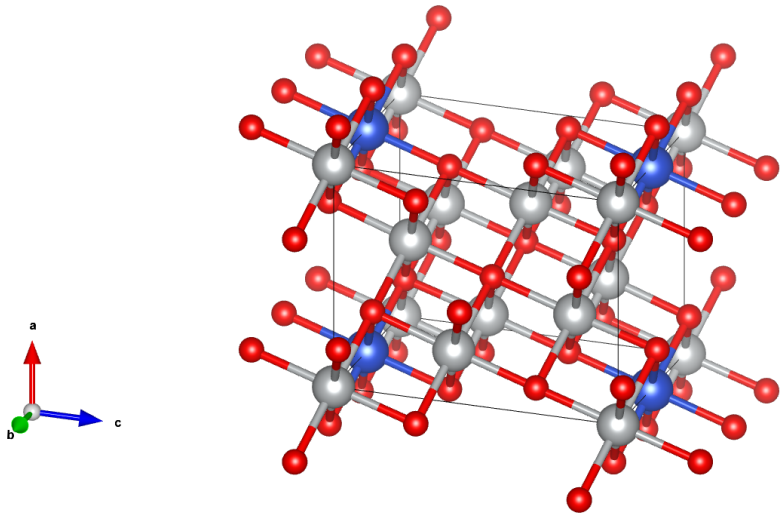

Fig. 5.3 The Ni_9CuO_{10} structure, with added bonds to showcase the crystal lattice. The nickel atoms are coloured in silver, copper in blue, and oxygen in red.

5.4 Conclusion

The doping convex hull for Ni-Cu-O was produced using the structures generated by Materials Project. There was only one compound discovered containing all three species that is on the hull itself, namely Ni_9CuO_{10}. This compound also had the lowest formation energy, producing an 'island of stability' within the ternary convex hull. This region would suggest that a 1:1 ratio of TM atoms to oxygen is the most stable configuration, with structures containing Cu in a 1:9 ratio to Ni being the most stable.

Chapter 6

Conclusion

6.1 Summary of Results

6.1.1 Bulk NiO

From simulating bulk NiO using the primitive cell, the comparison of RSCAN, PBE and PBE+U showed that while the electronic structure of RSCAN and PBE was similar, in order to obtain a realistic band gap, a Hubbard U value is needed. Additionally, the promising results for the electronic and optic band gap confirms the effectiveness of the linear response method of calculating the U value. Applying the Hubbard U value resulted in large changes to the band structure when compared to that of PBE and RSCAN. This effect demonstrates the increased localisation of the Ni 3d orbitals.

6.1.2 NiO Defects

NiO Vacancies

Studying the effect of vacancies showed the changes to the electronic structure of the supercell varied significantly around the band gap depending on which atom was removed. V_{Ni} showed a clear p-type semiconductor behaviour, which was expected from experimental results. By growing the sample in favourable conditions for oxygen vacancies, it is possible to narrow the band gap of NiO, push the material to a more n-type behaviour and cause increased localisation of Ni 3d orbitals.

1 and 2 Cu-Doped NiO Cells

The substitutional inclusion of Cu atoms into the structure again showed significant electronic variations within the band gap depending on the substituted atom. As expected, Cu_O and Cu_i exhibited more n-type behaviour than Cu_{Ni}. The comparatively more p-type behaviour of Cu_{Ni} would suggest that if Cu-doped NiO is to be used as a hole transport layer in photocathodes, the material would need to be synthesised in conditions that are favourable for the production of Cu_{Ni} defects.

The Cu_i defect caused significant disruption to neighbouring Ni atoms, resulting in highly spin-polarised states forming within the band gap. Furthermore, the numerous flat bands indicating increased Ni 3d orbital localisation would make this material more suited to investigation of exotic electronic states as a result of the increased electron-electron interaction.

By varying the positions of two Cu atoms within the supercell, the most favourable configuration would be the two Cu atoms being next to one another along the same [111] plane. This behaviour would hint at the possibility of clustering and phase-separation of Cu atoms with NiO. Further to this, the AFM nature of the cell is likely to be significantly disrupted.

10% Cu-Doped NiO Cell

The 10% Cu-doped cell confirmed the idea that with increasing Cu atoms incorporated into the structure, the Cu 3d orbitals increasingly hybridise with the O 2p, leading to more states forming within the band gap. The crystal displays almost half-metal like behaviour, with spin-polarised states forming at the Fermi level on only one spin channel, with opposite spin values both above and below the Fermi level. The near complete breakdown of the semiconducting properties in this case suggest that in the 10% case, there will be a remarkable increase in the conductivity and charge transfer capabilities of the material. This would further suggest that the 10% Cu-doped cell would be more suitable for use as a hole transport layer than the 2% and 4% Cu-doped cells.

Optically, it is also apparent that the addition of the Cu atoms causes the optical properties to change enough that the absorption of photons of a smaller wavelength increases compared to pure NiO. This is a key finding if this material is to be used in photocathodes due to the fact that by doping NiO with Cu the photocathodes will potentially see an increase in efficiency from more photons being absorbed in the visible spectrum of light.

Ni-Cu-O Convex Hull

The Ni-Cu-O convex hull revealed how copper prefers to be incorporated into a crystal lattice containing Ni and O. The most stable compound being Ni_9CuO_{10} showed a preference for both Ni and Cu to be in a 1:1 ratio with O, thus agreeing with previous experimental work on doping NiO. The Ni_9CuO_{10} compound is almost FCC in structure, with the three species forming bond angles at approximately 90°.

6.2 Future Avenues of Research

Extreme Doping Concentrations

There is a clear path of progression for future research, with systems of doping concentrations >10% being of great interest. Extreme doping concentrations with both Cu_{Ni} and Cu_O sites could be used to study the energetics of how the copper atoms preferentially place themselves given such a high doping concentration.

Phonon Calculations

Another possibility is the study of thermo-electric properties of Cu-doped NiO. Phonon calculations are orders of magnitude more expensive than spectral calculations however, and thus a much smaller supercell than studied in this thesis would have to be considered. CASTEP currently only supports the use of the finite displacement phonon calculation method for ultrasoft pseudopotentials and spin-polarised calculations for primitive and supercell calculations.

Convex Hull

All structures plotted in figure 5.2 were carried out without spin. As nickel atoms have spin, there is the possibility that magnetic structure searching could be carried out. Furthermore, the convex hull calculation in this study was carried out using the high-throughput pseudopotential library 'QC5', which is effective for its purpose, however a repeat of this study using a less-soft ultrasoft pseudopotential library will give a more accurate representation of the formation energies of the generated structures.

The dependence of the XC-functional used is worthwhile investigating. A comparison of the mGGA results with that of GGA/GGA+U could result in different stable phase predictions.

Other Dopant Species

Another possibility would be investigating how other transmission metals will affect the electronic properties of NiO. There have been a number of experimental studies in cobalt doping, studying electronic and optical properties [63]. Cobalt is magnetic, and thus will have a large effect on the Ni atoms around it. This could be particularly interesting when Co is added substitutionally in an O site, or even intrinsically as this will presumably cause a large amount of disruption to the magnetic spin structure of the material. Other metals could also be studied, such as the group one metals like potassium and sodium.

TDDFT

Another possible study would be to more accurately simulate the optical properties of the material. The more sophisticated method of TDDFT could be used here. These calculations would be extremely computationally expensive, however the use of a smaller supercell would possibly enable the use of this method.

References

[1] A. Dodd, A. McKinley, T. Tsuzuki, and M. Saunders, Materials Chemistry and Physics **114**, 382 (2009).

[2] A. Abbaspour-Tamijani et al., Applied Surface Science **515**, 145865 (2020).

[3] M. Nakayama, S. Yamada, R. Jalem, and T. Kasuga, Solid State Ionics **286**, 40 (2016).

[4] J. Linnera and A. J. Karttunen, Physical Review B **100**, 144307 (2019).

[5] G. Srinivasan and M. S. Seehra, Physical Review B **29**, 6295 (1984).

[6] E. Aytan et al., Applied Physics Letters **111**, 252402 (2017).

[7] J. Y. Zhang et al., Journal of Materials Chemistry C **6**, 2275 (2018).

[8] P.-C. Chen and S.-H. Yang, ACS Applied Energy Materials **2**, 6705 (2019).

[9] A. Rahdar, M. Aliahmad, and Y. Azizi, Journal of Nanostructures **4**, 145 (2014).

[10] M. Keikhaei and M. Ichimura, Semiconductor Science and Technology **35**, 035020 (2020).

[11] X. Zhou et al., Applied Surface Science **584**, 152651 (2022).

[12] Y. Wang et al., RSC Advances **12**, 21940 (2022).

[13] E. Schrödinger, Physical Review **28**, 1049 (1926).

[14] R. Zahradník and R. Polák, The time-independent schrödinger equation, in *Elements of Quantum Chemistry*, pages 13–46, Springer US, 1980.

[15] M. Born and R. Oppenheimer, Annalen der Physik **389**, 457 (1927).

[16] R. M. Martin, Electronic structure: Basic theory and practical methods, page 132, Cambridge University Press, 2020.

[17] P. Hohenberg and W. Kohn, Physical Review **136**, B864 (1964).

[18] W. Kohn and L. J. Sham, Physical Review **140**, A1133 (1965).

[19] D. S. Sholl and J. A. Steckel, Density functional theory: A practical introduction, pages 12–13, Wiley, 2009.

[20] R. Q. Hood, M. Y. Chou, A. J. Williamson, G. Rajagopal, and R. J. Needs, Physical Review B **57**, 8972 (1998).

[21] J. P. Perdew, K. Burke, and M. Ernzerhof, Physical Review Letters **77**, 3865 (1996).

[22] J. Sun et al., Nature Chemistry **8**, 831 (2016).

[23] A. P. Bartók and J. R. Yates, The Journal of Chemical Physics **150**, 161101 (2019).

[24] H. Sato, T. Minami, S. Takata, and T. Yamada, Thin Solid Films **236**, 27 (1993).

[25] H. Yang, Q. Tao, X. Zhang, A. Tang, and J. Ouyang, Journal of Alloys and Compounds **459**, 98 (2008).

[26] F. Roccaforte et al., Applied Surface Science **256**, 5727 (2010).

[27] V. I. Anisimov, J. Zaanen, and O. K. Andersen, Physical Review B **44**, 943 (1991).

[28] G. Moynihan, G. Teobaldi, and D. D. O'Regan, Physical Review B **94**, 220104 (2016).

[29] B. Himmetoglu, A. Floris, S. de Gironcoli, and M. Cococcioni, International Journal of Quantum Chemistry **114**, 14 (2013).

[30] P. Giannozzi et al., Journal of Physics: Condensed Matter **21**, 395502 (2009).

[31] M. Cococcioni and S. de Gironcoli, Physical Review B **71**, 035105 (2005).

[32] F. Bloch, Zeitschrift für Physik **52**, 555 (1929).

[33] W. Kohn and N. Rostoker, Physical Review **94**, 1111 (1954).

[34] P. Soven, Physical Review **156**, 809 (1967).

[35] S. J. Clark et al., Zeitschrift für Kristallographie - Crystalline Materials **220**, 567 (2005).

[36] A. J. Morris, R. J. Nicholls, C. J. Pickard, and J. R. Yates, Computer Physics Communications **185**, 1477 (2014).

[37] I. V. Solovyev, Physical Review B **103**, 104428 (2021).

[38] A. Jain et al., APL Materials **1**, 011002 (2013).

[39] A. K. Cheetham and D. A. O. Hope, Physical Review B **27**, 6964 (1983).

[40] C. Rödl, F. Fuchs, J. Furthmüller, and F. Bechstedt, Physical Review B **79**, 235114 (2009).

[41] I. Timrov, N. Marzari, and M. Cococcioni, Computer Physics Communications **279**, 108455 (2022).

[42] Y. Hinuma, G. Pizzi, Y. Kumagai, F. Oba, and I. Tanaka, Computational Materials Science **128**, 140 (2017).

[43] A. Togo and I. Tanaka, `Spglib`: a software library for crystal symmetry search, 2018.

[44] A. M. Ganose, A. J. Jackson, and D. O. Scanlon, Journal of Open Source Software **3**, 717 (2018).

[45] N. D. Browning, I. Arslan, R. Erni, and B. W. Reed, Low-loss EELS in the STEM, in *Scanning Transmission Electron Microscopy*, pages 659–688, Springer New York, 2010.

[46] J. Silcox, Current Opinion in Solid State and Materials Science **3**, 336 (1998).

[47] P. Ewels, T. Sikora, V. Serin, C. P. Ewels, and L. Lajaunie, Microscopy and Microanalysis **22**, 717 (2016).

[48] P. L. Potapov, S. E. Kulkova, D. Schryvers, and J. Verbeeck, Physical Review B **64**, 184110 (2001).

[49] J. C. Conesa, The Journal of Physical Chemistry C **120**, 18999 (2016).

[50] M. D. Irwin, D. B. Buchholz, A. W. Hains, R. P. H. Chang, and T. J. Marks, Proceedings of the National Academy of Sciences **105**, 2783 (2008).

[51] L. G. Ferreira, M. Marques, and L. K. Teles, Physical Review B **78**, 125116 (2008).

[52] P. Błoński and J. Hafner, Journal of Physics: Condensed Matter **21**, 426001 (2009).

[53] H. Ikeno and T. Mizoguchi, Journal of Electron Microscopy **66**, 305 (2017).

[54] J. Osorio-Guillen, S. Lany, A. Zunger, M. Caldas, and N. Studart, Nonstoichiometry and hole doping in nio, in *AIP Conference Proceedings*, AIP, 2010.

[55] S. Lany and A. Zunger, Physical Review B **78**, 235104 (2008).

[56] K. O. Egbo, C. E. Ekuma, C. P. Liu, and K. M. Yu, Physical Review Materials **4**, 104603 (2020).

[57] X. Zhang and X. Du, New Journal of Chemistry **44**, 1703 (2020).

[58] W. R. Meier et al., Physical Review B **102**, 075148 (2020).

[59] D. Misra and S. K. Yadav, The European Physical Journal B **94**, 76 (2021).

[60] M. C. Nguyen et al., Journal of Alloys and Compounds **732**, 567 (2018).

[61] C. J. Pickard and R. J. Needs, Journal of Physics: Condensed Matter **23**, 053201 (2011).

[62] M. Evans and A. Morris, Journal of Open Source Software **5**, 2563 (2020).

[63] R. Sharma et al., Materials Science in Semiconductor Processing **23**, 42 (2014).

[64] J. Madsen and T. Susi, Microscopy and Microanalysis **26**, 448 (2020).

[65] A. Hjorth Larsen et al., Journal of Physics: Condensed Matter **29**, 273002 (2017).

[66] E. J. Kirkland, Advanced computing in electron microscopy, pages 162–170, Springer International Publishing, 2020.

[67] D. Su, M. Ford, and G. Wang, Scientific Reports **2**, 924 (2012).

Appendix A

Miscellaneous Figures

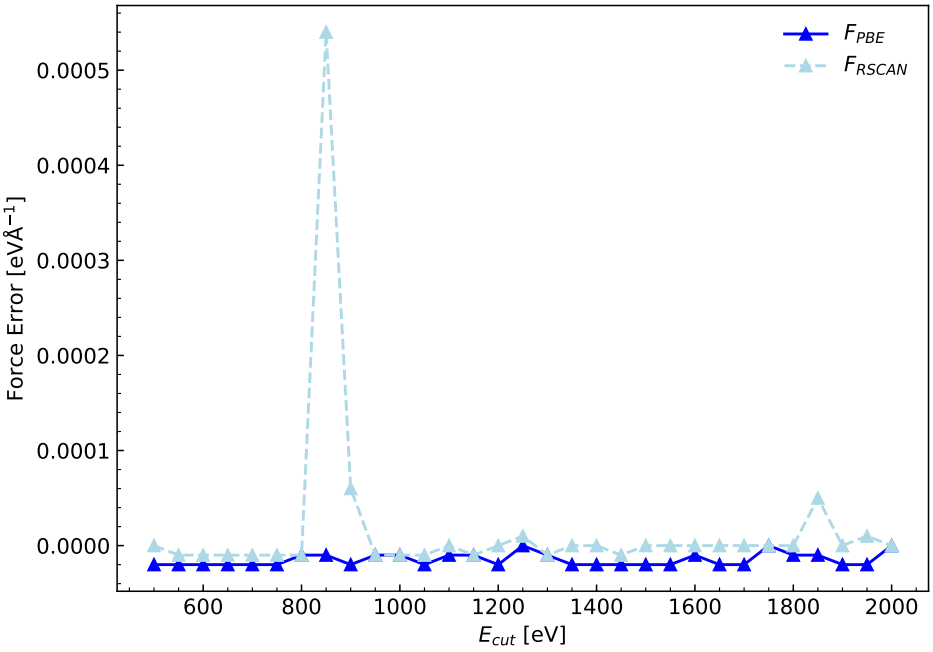

Fig. A.1 Force convergence error with increasing cut-off energies. The energy convergence tolerance of 10^{-8} eV and force convergence of 10^{-3} eVÅ^{-1} was applied.

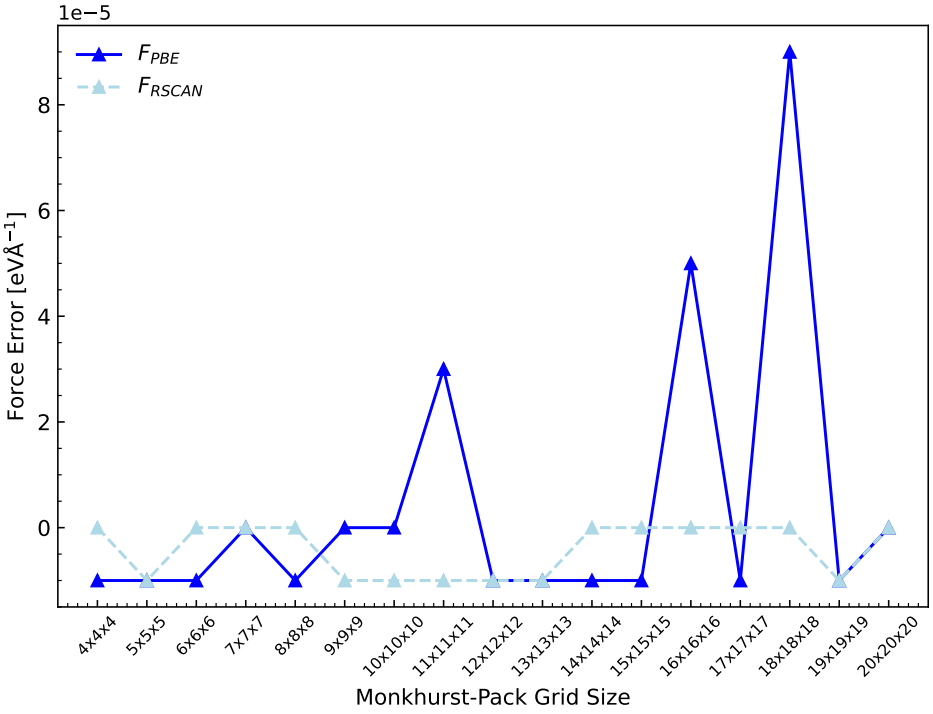

Fig. A.2 The force convergence error with increasing k-point grid density. The energy convergence tolerance of 10^{-8} eV and force convergence of 10^{-3} eVÅ^{-1} was applied.

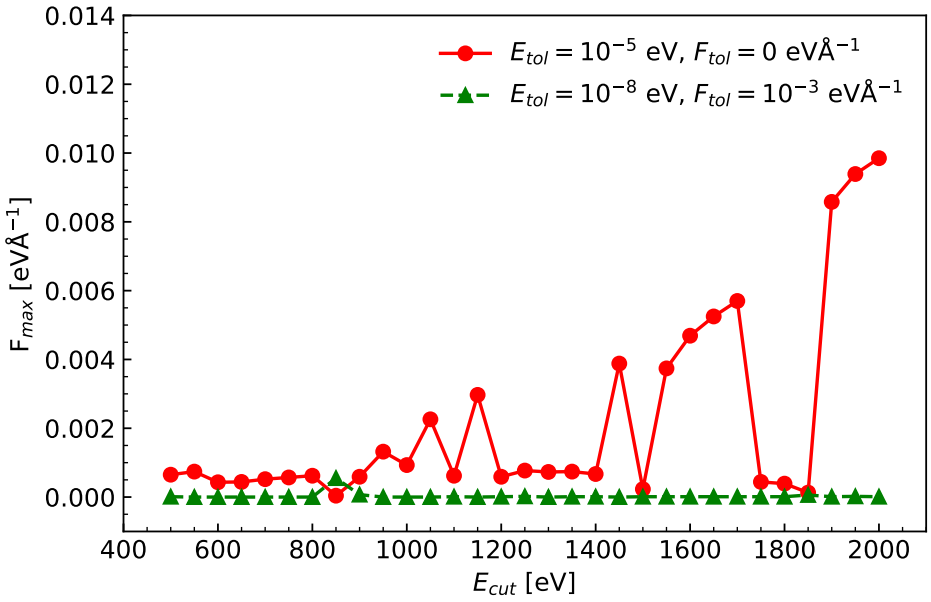

Fig. A.3 Magnitude of internal forces from NiO primitive cell using RSCAN.

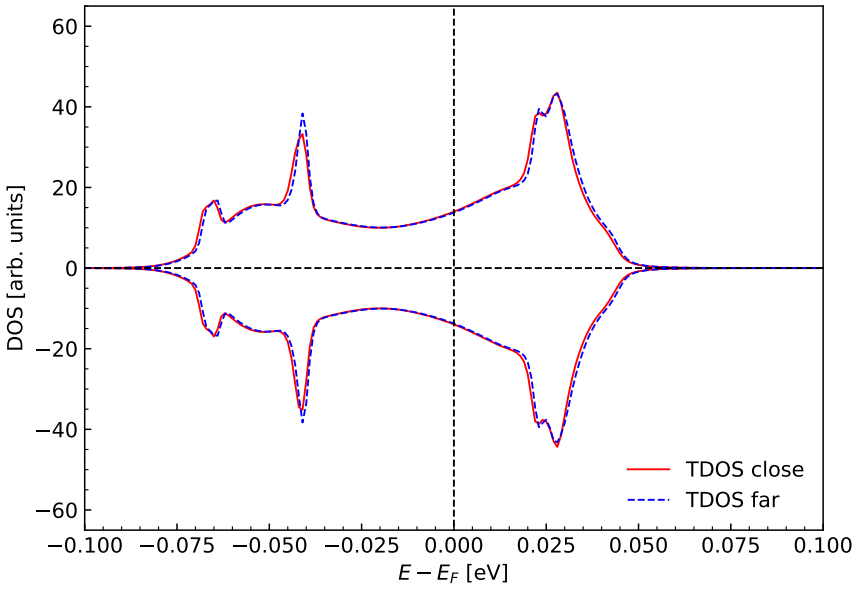

Fig. A.4 A comparison of the TDOS for small and large separation distances of two Cu_{Ni} defects.

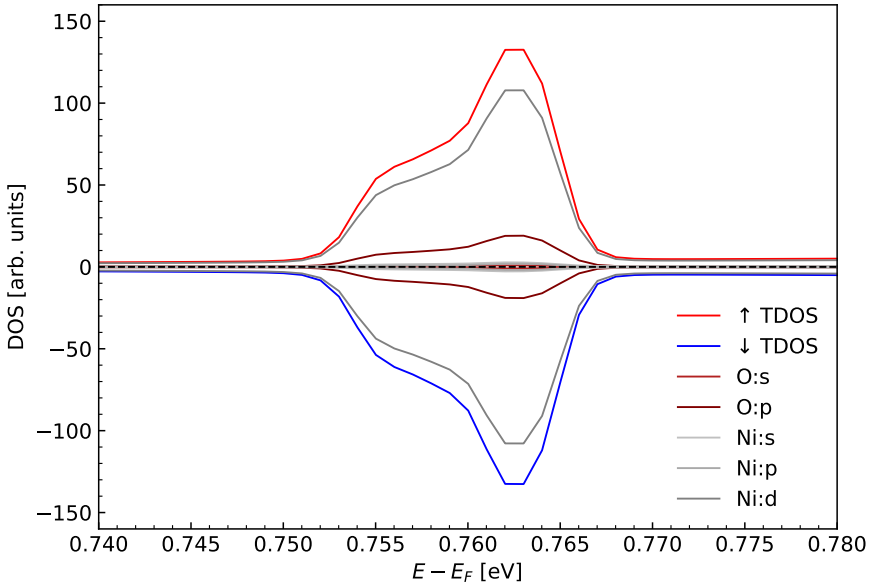

Fig. A.5 Decomposed PDOS composition of the flat band for V_O.

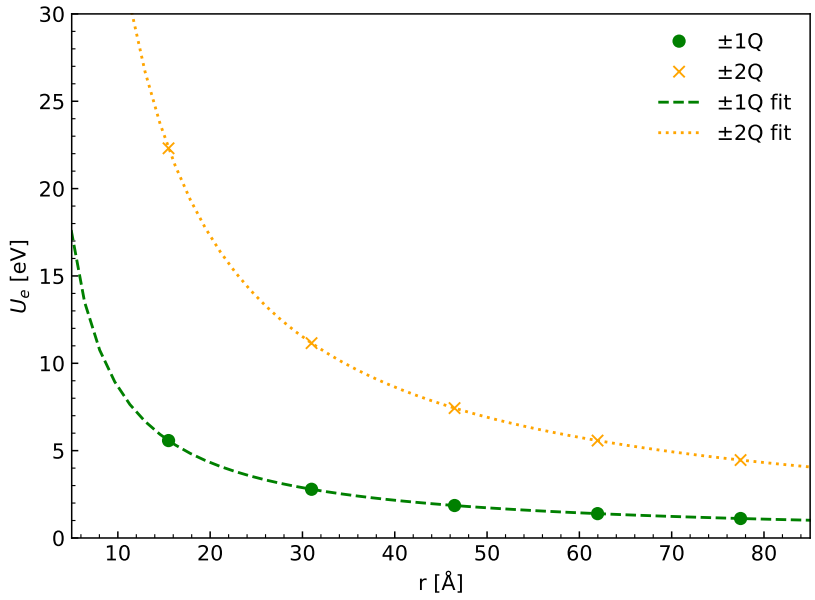

Fig. A.6 Comparison in Coulomb repulsion energies between a singly and doubly charged defect at different separation distances. Only the interaction between the original defect and the next repeated cell defects are considered.

Appendix B

Computational Microscopy Using abTEM

B.1 Introduction

There has been great interest in collecting TEM and STEM data for doped TMOs to investigate phenomena such as phase separation and defect formation. These systems can be quickly and easily modelled, with some limitations, as periodic supercells. These cells can be relaxed, as has been carried out many times during this study in previous chapters. TEM and STEM images can then be simulated from these structures using one of various programs that can solve the multislice equation, providing the plane-wave exit wavefunction.

The program used in this study is the Python module *ab initio* Transmission Electron Microscopy (abTEM) [64]. This is a powerful tool that can not only solve for the plane-wave exit wavefunction of an electron beam, but can also compute diffraction patterns and apply contrast transfer function (CTF) effects, such as phase aberrations, defocus and aperture effects. The program is able to simulate both TEM and STEM images, with cells being loaded in using the Atomic Simulation Environment (ASE) package [65]. The cells can then be tiled in all three dimensions to better model a thin film on a substrate.

B.2 The Mulitslice Equation

The wavefunction for n slices of a crystal surface is given by

$$\psi_{n+1}(x,y) = p_n(x,y,\Delta z_n) \otimes [t_n(x,y)\psi_n(x,y)] + \vartheta(\Delta z^2) \tag{B.1}$$

where $\psi_{n+1}(x,y)$ is the exit slice wavefunction, $p_n(x,y,\Delta z_n)$ is the propagator function, $t_n(x,y)$ is the slice thickness, $\psi_n(x,y)$ is the slice wavefunction, and the final term contains the error

introduced by the various approximations involved with the construction of the equation [66]. This error term is not included in the implementation of the multislice algorithm in computer codes.

B.3 Computational Methodology

The most important initial stage was the relaxation of a cell suitable for multislice calculation. To this end, the $2\times2\times2$ FCC supercell of NiO was chosen. This cell was also doped with two Cu atoms and relaxed using the same basis set. The basis set used was 800 eV, with a $6\times6\times6$ k-point grid density. The relaxed structures were then imported into the python script using the ASE structure importer.

These cells were then modified to create a surface. It was decided to investigate the [110] surface, as this is often imaged in actual experiments on NiO [67]. Each of these surfaces were tiled in the z direction, producing 4 layers, equalling a thickness of approximately 50 Å. A plane-wave energy of 300 keV was chosen to simulate the TEM electron beam.

The exit plane-wave additionally had contrast-transfer function (CTF) effects applied to the image to simulate aberrations.

B.4 Results and Discussion

B.4.1 6% Cu-doped NiO TEM

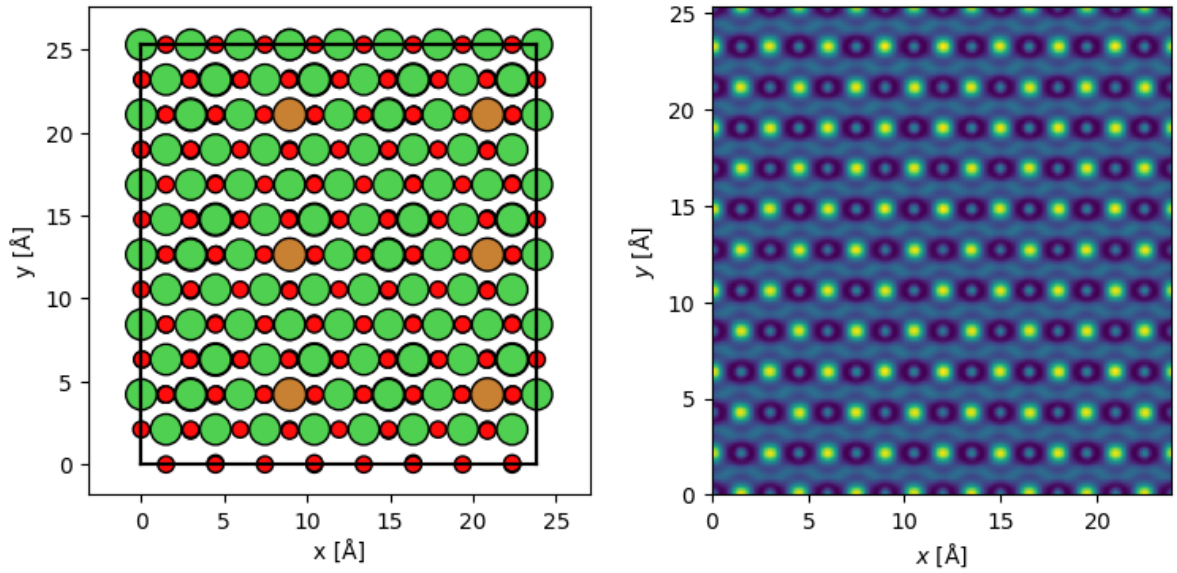

Fig. B.1 The Cu-doped NiO [110] surface simulated TEM image. Nickel atoms are shown in green, copper in brown, and oxygen in red. A beam energy of 300 keV was used, with CTF effects also being applied.

The TEM image with applied CTF effects and simplified atomic potential for the Cu_{Ni} case showed that the copper atoms are so similar to the nickel atoms that being able to differentiate them is impossible.

B.4.2 6% Cu-doped NiO STEM

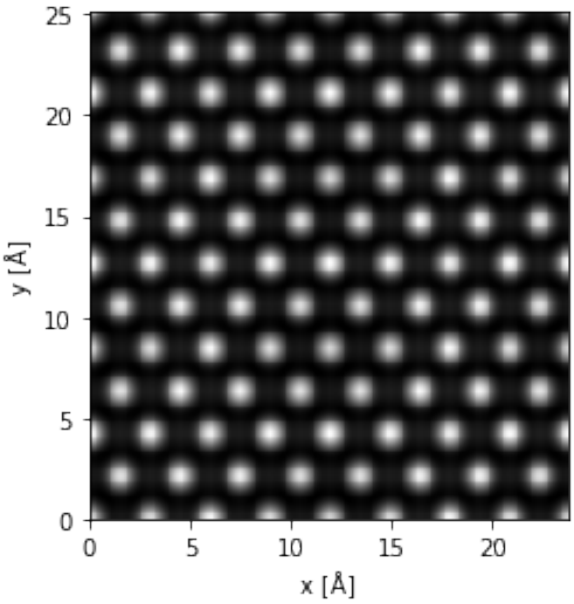

Fig. B.2 The Cu-doped NiO [110] surface simulated STEM image. A beam energy of 80 keV was used, with CTF effects applied.

The STEM image of the surface shows copper/nickel positions with much higher contrast compared to TEM. Unfortunately, there is still very little difference between the copper and nickel atoms and thus there is very little in the way of crystal structure distortion and visual difference between the two metals.

B.5 Conclusion

The TEM simulation studies of Cu_{Ni} doping cases showed that differentiating the copper from the nickel atoms in both TEM and STEM images will be of great difficulty. Future studies could be conducted into other defect types with more disrupted structures, such as Cu_O or Cu_i.